Three-Dimensional Tailored Vibration Response and Flutter Control of High-Bypass Shroudless Aeroengine Fans

O. G. McGee III
Professor

C. Fang
Postdoctoral Research Associate

Howard University,
Washington, DC 20059

A new reduced-order design synthesis technology has been developed for vibration response and flutter control of cold-stream, high-bypass ratio, shroudless, aeroengine fans. To simplify the design synthesis (optimization) of the fan, a significant order reduction of the mechanical response and stiffness-shape design synthesis has been achieved. The assumed cyclic symmetric baseline fan is modeled as a cascade of tuned, shroudless, arbitrarily shaped, wide-chord laminated composite blades, each with a reduced order of degrees of freedom using a three-dimensional (3D) elasticity spectral-based energy model (McGee et al., 2013, "A Reduced-Order Meshless Energy Model for the Vibrations of Mistuned Bladed Disks—Part I: Theoretical Basis, ASME J. Turbomach., in press; Fang et al., 2013, "A Reduced-Order Meshless Energy Model for the Vibrations of Mistuned Bladed Disks—Part II: Finite Element Benchmark Comparisons, ASME J. Turbomach., in press). The uniqueness of the mechanical analysis is that the composite fan was modeled as a "meshless" continuum, consisting of nodal point data to describe the arbitrary volume. A stationary value of energy within the arbitrarily shaped composite fan annulus was achieved using an extended spectral-based Ritz procedure to obtain the dynamical equations of motion for 3D free vibration response of a rotating composite high-bypass fan. No additional kinematical constraints (as in beam, plate, or shell theories) were utilized in the 3D elasticity-based energy formulation. The convergence accuracy of the spectral-based 3D free vibration response predictions was nearly one percent upper-bounds on the exact mechanical response of the baseline composite fan, particularly in the lowest five modes studied closely in this work, as typically seen with spectral-based Ritz procedures employed in the analysis. The spectral-based 3D predictions was validated against those predicted using a general purpose finite element technology widely used by industry. In off-design operation, the frequency margins of the lower flex-torsion modes of a fan may be dangerously close to integral-order resonant and empirical stall flutter boundaries. For a given baseline composite fan, it is proposed that to reduce the likelihood of resonant response and flutter on a Campbell diagram, design analysts can efficiently unite the newly developed reduced-order 3D spectral-based energy reanalysis within a novel reduced-order spectral-based Kuhn–Tucker optimality design synthesis procedure to fairly accurately restructure the Campbell diagram of a composite high-bypass ratio fan using stiffness optimization (by means of proper choices of angle-ply orientations of the blade laminates) and mass-balancing (shape) optimization (by way of blade thickness variation tuning of the lower aerodynamic loading portion of the blades between the dovetail root section and the midradial height section of the composite fan annulus). Fan design optima is summarized that (1) achieves multiple frequency margins and satisfies multiple empirical stall flutter constraints, (2) controls the twist-flex vibratory response in the lowest (fundamental) mode, and (3) ensures the mechanical strength integrity of the optimized angle-ply lay-up under steady centrifugal tension and gas bending stresses. Baseline and optimally restructured Campbell diagrams and design sensitivity calculations are presented, comparing optimum solution accuracy and validity of the proposed reduced-order spectral-based design synthesis technology against optimum solutions generated from open-source nonlinear mathematical programming software (i.e., NASA's general-purpose sequential unconstrained minimization technique, Newsumt-A) (Miura and Schmit, Jr., 1979, "NEWSUMT–A, Fortran Program for Inequality Constrained Function Minimization—Users Guide," NASA CR-159070). Design histories of fan stiffness and mass balancing (or shape) along with nondimensional constraints (i.e., frequency margins, reduced frequencies, twist-flex vibratory response, first-ply failure principal stress limits, and dovetail-to-midblade height thickness distribution) show that a proper implementation of fan stiffness tailoring (via symmetric angle-ply orientations) and mass-balancing (thickness) optimization of the fan assembly produces a feasible Campbell diagram that satisfies all design goals. An off-design analysis of the optimized fan shows little sensitivity to twist-flex coupling response and flutter with respect to small variability or errors in optimum design construction.

Contributed by the Technical Committee on Vibration and Sound of ASME for publication in the JOURNAL OF VIBRATION AND ACOUSTICS. Manuscript received January 5, 2009; final manuscript received July 25, 2011; published online March 18, 2013. Assoc. Editor: Jiong Tang.

*Industry manufacturing processes may introduce these small errors known as angle-ply laminate construction misalignments (Graham and Guentert, 1965, "Compressor Stall and Blade Vibration," Aerodynamic Design of Axial-Flow Compressors, Chap. XI, NASA SP-36; Meher-Hornji, 1995, "Blading Vibration and Failures in Gas Turbines, Part A: Blading Dynamics and the Operating Environment," ASME Paper 95-GT-418; Petrov et al., 2002, "A New Method for Dynamic Analysis of Mistuned Bladed Disks Based on the Exact Relationship Between Tuned and Mistuned Systems," ASME J. Eng. Gas Turbines Power, **124**(3), pp. 586–597; Wei and Pierre, 1990, "Statistical Analysis of the Forced Response of Mistuned Cyclic Assemblies," ASME J. Eng. Gas Turbines Power, **28**(5), pp. 861–868; Wisler, 1988, "Advanced Compressor and Fan Systems," GE Aircraft Engines, Cincinnati, Ohio (also 1986 Lecture to ASME Turbomachinery Institute, Ames Iowa)).* [DOI: 10.1115/1.4006758]

1 Introduction

Modern bypass aeroengines have numerous high-energy rotating components, which are designed for maximum thrust and propulsive efficiency and minimum weight. However, it is the cold stream fan with its high axial flow and low pressure ratio which bestows industry with persistent design questions. An ongoing question is how to design lightweight blades that deliver improved mechanical performance, whose construction is capable of withstanding the damage by foreign objects and erosive elements. The large diameter of modern high-bypass engine fans (say over 10 ft (3.048 m)) creates an enormous penalty on engine weight. Conventional fan designs have incorporated a large number of long, narrow chord blades. These high aspect ratio blades typically have natural vibration frequencies, which may cause instabilities and resonances to occur within the normal engine operating range.

To prevent fatigue failures caused by flutter and resonant response, conventional blades are coupled at their tips or at an intermediate radius by shrouds. As the fan rotates, shrouds on neighboring blades effectively join into a stiffened ring around the fan assembly. This mechanical stiffness redistribution tends to shift the more complex blade-shroud natural frequencies out of the troublesome range. Unfortunately, the shrouds also reduce the fan's aerodynamic efficiency. Hence, a fan design that dispenses with shrouds has a significant performance advantage.

One way to eliminate the shrouds is to make the fan blades stiffer by reducing the number of blades and increasing the blade chord from hub to tip (see Fig. 1). Each fan blade then is inherently stiffer and the aerodynamic efficiency is improved. Yet, such a fan would also be quite heavy, if constructed monolithically of solid metal. An earlier proposed solution has been to construct the blades using lightweight construction, such as laminated, polymer matrix composites or viscoelastic layers, or even modern functionally graded materials. Future lightweight construction, wide chord fan blades may be directionally stiff, energy efficient and, with the proper construction techniques, reasonably durable in operation and serviceable life.

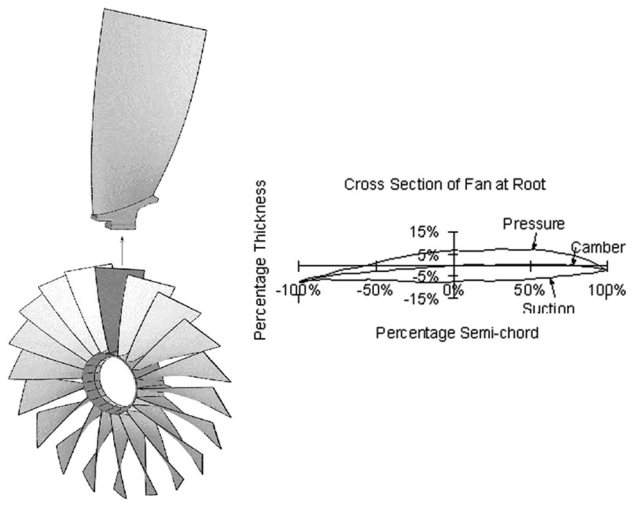

Fig. 1 Cyclic symmetric view of the composite bypass engine fan assembly 3D model analyzed

Aeroelasticity considerations in shroudless, high-bypass fan design continue to pace the technology [1,2]. Recent employments in bypass aeroengines have caused designers to be more concerned about their mechanical integrity in off-design operation. Inside the range of the lower harmonics of the shaft frequency (say within 1–4 per rev) these fans typically experience flex-torsion mode instability and forced response inducing high-cycle fatigue and eventual blade damage or destruction. Typical blade damage severities are either loss of the entire airfoil and/or airfoil dovetail in the coupled first flex and first torsion modes, or breakage of the outer portion of the airfoil in the coupled second flex and second torsion modes. In either of these cases significant replacement and repair costs are warranted; as a result of annulus unbalance and/or ingestion damage to downstream engine components.

To eliminate this damage, a largely experienced-based approach for judging acceptable composite fan designs is to avoid flex-torsion frequency synchronization with low-order harmonics of the shaft frequency (i.e., engine orders) on a Campbell diagram [3,4]. The engine speeds at which such frequency synchronizations take place are called *critical speeds*. At such speeds, resonant fatigue is the primary blade failure mechanism as a result of *integral order forced response*. Integral order response originates either from periodic excitations mechanically induced or from aerodynamic distortions asymmetrically and periodically applied within the fan blade passages [5–11], causing synchronous vibrations at fan natural frequencies, as well as nonsynchronous vibrations [12] away from fan natural frequencies. The latter aerodynamic distortions may result from passage of the fan assembly through nonuniform flow disturbances, such as inlet distortion, from shock-induced disturbances within the blade row, or from end wall boundary layer and secondary flow effects near the hub and tip regions. A possible source of high vibratory stress, which occurs at frequencies not synchronous with the shaft frequency, is known as *nonintegral order response*. Such response may be the result of choke stall, common at lower speeds and pressure, or of stall flutter, primarily at higher speeds and pressure.

Enabling fan technologies call for the use of passive mechanisms of tailored vibration response and flutter control. Such passive control can be achieved by adjusting the stiffness of the fan through shape tailoring and/or material redistribution. In off-design operation, the frequency margins of the lower flex-torsion modes of a fan may be dangerously close to integral-order resonant and empirical stall flutter boundaries. It is shown that a proper construction of fan stiffness tailoring and shape (thickness)

optimization from dovetail-to-midradial height can be found to reduce the likelihood of resonant response and flutter on a Campbell diagram [4].

The present approach employs passive stiffness control that assumes the fan blades ideally constructed of matrix composites layers, and that assumes the fan blades can be tailored by a proper choice of thickness from dovetail-to-midradial height. These composites were assumed to be made of a graphite-epoxy material, because of its high tensile strength per unit mass (nearly 2.5 psi/lb $in^{-3} \times 10^6$), particularly when operating temperatures fall in the range of 50–500 °F. Ideally, the polymer matrix composites used were combined to form a symmetrically laminated composite to eliminate coupled tension-flexure and coupled tension-shear blade response [13–15]. Coupled twist-flexure blade response occurred when the composites was stacked at noninteger-valued angle-ply orientations in the range of 0 deg to $\pm$90 deg. Unavoidable fabrication imperfections of symmetric laminates (such as ply misorientations, fiber migrations, and nonuniformities) can produce additional coupled blade response in the presence of residual stresses and aeromechanical loads [16,17].

Vibration-resistant and flutter-free high-bypass fans depend on developing reduced-order fan system models utilizing constrained design synthesis or optimization technology. For practical reasons, such design technology must include efficient modeling capabilities for fan assemblies with arbitrarily shaped blades having radially varying sweep and thin variable sections, and constructed monolithically of solid metal or polymer matrix composite laminates or viscoelastic layers. In addition, a robust design synthesis technology must include a number of design variables, either aerodynamically or mechanically classified, which may be useful in controlling fan instability and response. These include Mach number, number of blades, flow incidence, shock position, reduced velocity, damping, thickness, chord width, edge radii, and mode shape, just to name a few.

The underlying principle in composite bypass fan flutter control is reducing twist-flex coupling, induced both mechanically and aerodynamically, as much as possible so that the twist-flex responses become in the limit predominately independent of one another. Provided adequate twist-flex damping is copious, as it will be for small angles of flow incidence to the fan, classical flutter can be amply suppressed. Twist-flex coupling response will be coupled by composite ply-layup and also by blade cross-sectional product moment of inertia distribution along the fan annulus radial height. It is possible to arrange the mass (or optimize the shape, i.e., thickness and/or chord width) of the composite bypass fan in such a manner that the radial height distribution of blade section product moment of inertia nearly vanishes, resulting in a near mass-balanced composite bypass fan. For such a fan a predominately twist (or flex) oscillation may be induced in the flow stream without a tendency to generate the other kind of predominate motion. For steady oscillations predominately twist (or flex) responses in a suitably arranged mass-balanced composite bypass fan are approximately in-phase with one another. However, twist-flex coupled response is not in-phase with the twist motion trailing considerably behind the flex motion. Largely depending on the twist-flex elastic stiffnesses of the composite bypass fan, a proportional increase of the twist-flex stiffness lower the critical reduced frequencies approximately in proportion to the square-root of twist-flex stiffness.

In relation to employing a practical method of flutter suppression, the coupling in the flexural moments cannot be completely eliminated, because aerodynamic coupling due to blade pretwist in the torsional motion is necessarily present. As a consequence of additional angle of incidence, the torsional motion itself aims to either dissipate out or supplement in. Nonetheless, torsion does continue to affect, elastically and inertially, composite fan flexure. Thus, the radial distribution of fan pretwist may be assumed averaged such that the angle of incidence along the radial height of the bypass fan is zero consistent with customary modus operandi of fan vibration control used by industry designers.

The foregoing argument suggests that flutter may be suppressed when the flexural center coincides with the center of twist-flex independence and the composite fan is mass balanced about this common center. There is, however, some tolerance on the mass balance and position of the flexural center, so that flutter may still be suppressed when the ideal conditions are not exactly satisfied. Even when these conditions are seriously contravened, the critical reduced frequency may be away from empirical constraints, and this can optimally be ensured by designing the torsional elastic stiffness of the composite fan sufficiently large, pushing the first torsional frequency sufficiently high as possible on a Campbell diagram [4].

Outside classical flutter—which is oscillations in which composite bypass fan twist-flex coupling persists causing the instability—stall flutter—which is oscillations in either predominately twist or predominately flex motions—arises from aerodynamic damping across the composite bypass fan changing from positive to negative. Largely induced by flow incidence, when the incidence angle is small, the fan is stable, and when the incidence is near the positive or negative stalling condition, self-excited oscillations may be induced. The exact mechanism of stall flutter is not fully understood. However, it is known to be associated with periodic flow separation and subsequent reattachment of the flow about the fan blade. Stall flutter cannot be prevented by mass-balancing measures, which tend to uncouple twist-flex motion. Stall flutter suppression is secured by arranging the reduced frequencies at any possible stalling condition constrained at or near empirically acceptable values. Empirical studies have disclosed at Reynolds numbers exceeding 2×10^6 stall flutter instabilities do not occur, if sufficient composite fan stiffness is provided for the twist-flex reduced frequencies—a nondimensional quantity proportional to the product of the twist-flex natural frequency and the blade chord, divided by the free stream speed—to exceed values empirically well-established for fan flutter suppression in practice.

A fan vibration suppression strategy developed in the present work is to tune the blade stiffness and mass balance with composite tailoring using a proper choice of angle-ply stacking along with an optimum design of blade thickness from the hub to near the mean radial height. This passive stiffness control strategy is approached, while at the same time, preserving the blade's basic aerodynamic profile characteristics (near the highly loaded tip region). The literature on the use of composite tailoring in aeronautical structures design [14,15,18–29] suggest the use of continuous-valued design variables, such as ply thicknesses, and more recently, of integer-valued cross-ply and angle-ply orientation angles, such as 0 deg, 90 deg, and $\pm$45 deg. The present high-bypass fan design synthesis and passive vibration suppression and flutter control strategy assumes blade models comprised of fixed-ply thicknesses, and symmetric angle-ply stacking sequences with noninteger-valued orientation angles ranging from 0 deg to $\pm$90 deg.

Conventional reduced-order aeroelastic technologies based solely on weight performance measures [27–30] may lead to fan designs with subordinate mechanical integrity having sufficient fan stiffness and mass balance than desirable, particularly in regards to experiential combinations of instabilities and resonances that may occur within the normal engine operating range. Improved three-dimensional high-fidelity reduced-order models of flutter, resonance stress, and high-cycle fatigue are required supplementing what is currently available [26,29–36] to achieve future advanced very high bypass fans with reduced weight. Better resonance stress suppression capability is also needed for such advanced fan designs. The motivation of the present work is to enhance model reduction technology of high-bypass fan design. The technology will improve the mechanical reliability of high-energy, rotating fan components in propulsion systems and ultimately, lower the incidence of high-cycle fatigue malfunctions and reduce the number of uncontained engine failures.

The paper takes a proof-of-concept design approach at fan vibration suppression and flutter control of a class of high-bypass

ratio, shroudless composite fans. Moreover, three overarching questions underpin this approach. These are: (1) Can suppression techniques of fan stiffness redistribution through material constants or composite tailoring and fan mass balancing by way of shape optimization (i.e., dovetail-to-midradial blade height thickness variation) be used to achieve prescribed frequency margins and empirical stall flutter boundaries, and to limit the twist-flex vibration response of high-bypass ratio shroudless fans? (2) To what degree of sensitivity does properly tailored stiffness and mass of fans alleviate excessive resonant vibrations, stall flutter instabilities, and twist-flex vibration response? (3) How does the mechanical response capability of the three-dimensional reduced-ordered technology of composite fan design developed in the present work compare to general-purpose finite element technology widely used by industry? (4) How does the global optimum solutions predicted for vibration suppression and flutter control of a certain class of high-bypass composite fan recently engaged by industry using the reduced-order spectral-based Kuhn–Tucker [37] design synthesis developed in the present study compare to local optimum solutions predicted for the composite fan using a widely used conventional method of nonlinear programming (i.e., NASA's general-purpose sequential unconstrained minimization technique, Newsumt-A [3])?

2 Objectives and Scope of Study

The objective of this study is to improve the model reduction technology of a class of high bypass ratio, shroudless fan design. The approach is to explore fan design stiffness tailoring and fan mass balancing via shape (thickness) optimization for flutter control and resonant stress suppression. To simplify the optimization of the fan, a significant order reduction of the mechanical analysis has been achieved. The assumed cyclic symmetric baseline fan is modeled as a cascade of tuned, shroudless, arbitrarily shaped, wide-chord blades, each with a reduced-order of degrees of freedom (DOF) using a three-dimensional (3D) elasticity-based, energy model [1,2].

A baseline fan is numerically optimized using a first-of-its-kind reduced-order spectral-based design synthesis involving a stationary condition solution of simultaneous nonlinear partial differential equations in the design variable space (i.e., angle-ply orientations, shape (thickness) tailoring, and conventional slack variables or Lagrange multipliers), comprising the necessary and sufficient Kuhn–Tucker conditions of optimality of constrained minimization. Solution accuracy and validity of the present reduced-order design synthesis technology is benchmarked against a widely used conventional method of nonlinear programming (via. sequential unconstrained minimization technique). A baseline fan Campbell diagram is optimally restructured with wider resonant frequency margins at low integral orders that (1) achieves multiple frequency margins while maintaining proper clearance from multiple empirical stall flutter boundaries, (2) controls twist-flex coupling at the blade tips in the lowest (fundamental) mode, and (3) ensures the mechanical strength integrity through maximum restrictions placed on steady centrifugal tension and to a lesser extent gas flow-induced bending stresses.

Results summarize design histories of fan stiffness (angle-ply lay-ups), fan shape (thickness), and nondimensional restrictions on frequency margins, reduced frequencies, twist-flex vibratory response, and first-ply failure principal stress limits. Finally, a practical assessment of the off-design sensitivity of fan design optima is performed. This assessment includes a consideration of manufacturing tolerances of ± 5 deg from optimum stiffness (angle-ply orientations) of the fan design. Such manufacturing disorders are shown to have very little effect on the optimality of the fan stiffness and shape tailoring (i.e., satisfaction of the cost function and constraints). An outgrowth of this optimization is a clearer understanding of the feasible design stiffness and mass-balancing shape for passive vibration and flutter suppression of shroudless fans used in cold-stream, high-bypass turbofan engines.

In the next section the reduced-order composite fan analysis model is described. This is followed by discussions of the geometric and material properties of the baseline design of a class of bypass fans. A convergence study of frequencies and mode shapes of the baseline fan is then presented to assess the accuracy of the 3D reduced-order fan vibration response model developed in previous and ongoing work [1,2]. In addition, a detailed 3D finite element-based mechanical analysis of the baseline fan is performed to compare its predictive accuracy against the present reduced-order energy-based mechanical analysis. A brief description is given about the objective function and the aeromechanical constraints associated with the present composite fan design problem. This is followed by a mathematical description of the optimization technique employing nonlinear programming via a sequential unconstrained minimization technique. After this, a definition of the necessary and sufficient conditions for global optimality of the fan design is presented. Next, the optimum design histories and off-design sensitivity analyses of the composite fan are summarized to evaluate the performance of the present design procedure in addressing the first two overarching questions of this paper. Finally, conclusions are offered which relate this work to the central query of instability and response suppression of high-bypass engine fans.

3 Reduced-Order Response Model of a Bypass Engine Fan

To simplify the optimization of the fan, a three-dimensional (3D) reduced-order meshless energy (ROME) fan response analysis model was developed. The fan was modeled as a tuned cascade of shroudless, wide chord blades. A 3D cyclic symmetric view of a tuned bypass engine fan assembly is shown in Fig. 1. Each of the blades were model with a reduced-order of degrees of freedom using a 3D elasticity-based, energy formulation [1,2] incorporating variable chord distribution, variable skewness, laminated orthotropy, full geometric nonlinearity using an updated Lagrangian material coordinate description, and including all centrifugal and Coriolis acceleration effects. The blade model (Fig. 2) was assumed clamped along the base of the dovetail and completely free on all other edges. A spectral-based Ritz variational procedure was used to obtain stationary values of the elastodynamic energies of the fan. The blade's 3D displacements (u,v,w) along the Cartesian coordinates (x,y,z) (Fig. 1) were approximated as a mathematically complete [38–40], generalized Fourier series of 3D orthonormal polynomials [1,2] satisfying assumed vanishing displacement conditions along the base of the dovetail.

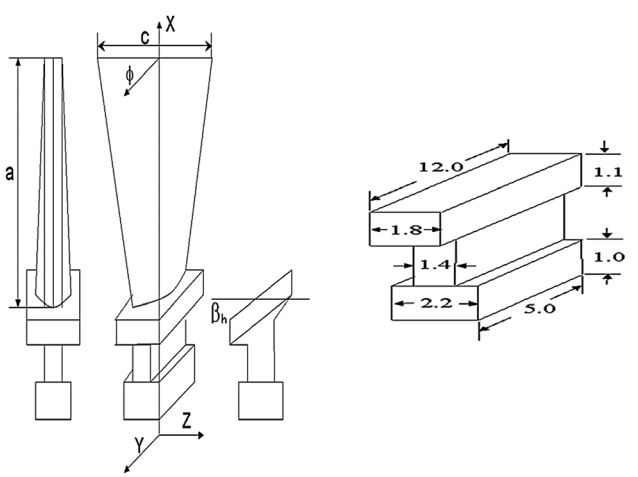

Fig. 2 Geometric dimensions (inches (in.) = 2.54 cm) of blade and dovetail 3D model analyzed ($\beta_H = 12.5$ deg)

The flow path was directed along the dovetail slope β_H (see Fig. 2). The reference dimensions of the blade are height a, dovetail slope chord $b_H = b\ \cos(\beta_H)$ (at $x = a_H$, the dovetail radial height), and tip chord c (at $x = a_T$, the tip radius), thickness t_h, and ply thickness t_p. Additional geometrical dimensions of the blade and dovetail modeled are shown in Fig. 2. The model assumed an arbitrary blade profile shape (e.g., double circular arc, multiple circular arc, NACA Series 65, British, grid-generated, etc.), as shown in Fig. 2.

3.1 Governing Energy Equations. The engineering strains $\{\varepsilon\}$ were related to the composite fan displacements, u,v,w, along the Cartesian coordinates, x,y,z (Fig. 1), as follows: $\{\varepsilon\} = \{\varepsilon_x, \varepsilon_y, \varepsilon_z, \gamma_{xy}, \gamma_{yz}, \gamma_{xz}\}^T = \{\varepsilon^L\} + \{\varepsilon^{NL}\}$, where $\{\varepsilon^L\}$ is the classical linear strain vector, and $\{\varepsilon^{NL}\}$ is the nonlinear geometric strain vector, incorporating the usual squares and products of the displacement gradients, e.g.,

$$\varepsilon_x = \frac{\partial u}{\partial x} + \frac{1}{2}\left[\left(\frac{\partial u}{\partial x}\right)^2 + \left(\frac{\partial v}{\partial x}\right)^2 + \left(\frac{\partial w}{\partial x}\right)^2\right];$$
$$\gamma_{xy} = \frac{\partial u}{\partial y} + \frac{\partial v}{\partial x} + \frac{\partial u}{\partial x}\frac{\partial u}{\partial y} + \frac{\partial v}{\partial x}\frac{\partial v}{\partial y} + \frac{\partial w}{\partial x}\frac{\partial w}{\partial y};\quad \text{etc.} \tag{1}$$

In addition, a linear elastic constitutive law (including monolithic or laminated composite construction) was assumed. Hence, the stress vector for the pth-ply was

$$\{\sigma^{(p)}\} = [Q^{(p)}]\{\varepsilon\} = \{\sigma^{(p)L} + \sigma^{(p)NL}\}^T\{\varepsilon^L + \varepsilon^{NL}\}, \tag{2}$$

where $\{\sigma^{(p)}\} = \{\sigma_x, \sigma_{y\ldots}\tau_{xz}\}^{(p)T}$, $\{\sigma^{(p)L}\} = [\mathrm{Q}^{(p)}]\{\varepsilon^L\}$ and $\{\sigma^{(p)NL}\} = [\mathrm{Q}^{(p)}]\{\varepsilon^{NL}\}$ was linear and nonlinear stresses of the pth ply, and $[\mathrm{Q}^{(p)}]$ was a matrix of stiffness coefficients for laminated orthotropy [41] involving the usual material constants E_{11}, E_{22}, E_{33}, G_{23}, G_{13}, G_{12}, ν_{12}, ν_{21}, ν_{23}, ν_{32}, ν_{13}, ν_{31}, and direction cosines $m = \cos\theta$ and $n = \sin\theta$, where θ was the angle-ply orientation. The deformation energy functional (U) of the composite fan incorporated in the proposed reduced-order spectral model was

$$\begin{aligned} U &= \frac{1}{2}\iiint \{\sigma^{(p)}\}^T\{\varepsilon\}dV \\ &= \frac{1}{2}\iiint \{\sigma^{(p)^L} + \sigma^{(p)^{NL}}\}^T\{\varepsilon^L + \varepsilon^{NL}\}dV \\ &= U_L + U_\sigma + U_{NL} \end{aligned} \tag{3}$$

whereas a differential volume is

$$dV = dx \times dy \times dz, \quad U_L = \frac{1}{2}\iiint \left\{\sigma^{(p)^L}\right\}^T\{\varepsilon^L\}dV \tag{4}$$

was the usual linear elastic deformation energy, and

$$U_\sigma = \frac{1}{2}\iiint \left\{\sigma_0^{(p)^L}\right\}^T\{\varepsilon^{NL}\}dV \tag{5}$$

defined the supplemental geometric nonlinear deformation energy due to tension-flexure coupling, where $\{\sigma_0^{(p)L}\}$ was the initial linear stress vector, and U_{NL} denoted higher-order deformation energy, which was neglected in the present ROME analysis. Dynamical energies included in the proposed reduced-order spectral model resulting from the temporal kinematics of the composite fan was the usual kinetic energy,

$$T_O = \frac{1}{2}\iiint \rho^{(p)}\ddot{\Delta}\ dV \tag{6}$$

additional kinetic energy due to centrifugal accelerations,

$$T_\Omega = \frac{1}{2}\iiint \rho^{(p)}\Delta^T[\Omega]\Delta dV \tag{7}$$

and supplemental energy due to Coriolis acceleration,

$$T_C = \iiint \rho^{(p)}\dot{\Delta}^T[R]\Delta dV \tag{8}$$

where the dot $(\cdot)$ indicates a derivative with respect to time t, $\rho^{(p)}$ is the mass density of the pth-ply of the composite fan blade, and $\Delta = \{u,v,w\}^T$ is a vector of Cartesian displacements. The $\{\Omega_x, \Omega_y, \Omega_z\}^T$ contained a vector of angular velocities of the composite fan rotating with respect to the global (x,y,z) coordinate system. Accordingly, the y axis was the rotating axis, the rotor speed was Ω, and the angular velocity vector was $\Omega\{0,1,0\}^T$, with $[\Omega] = [R]^T[R]$, where

$$[R] = \begin{bmatrix} 0 & -\Omega_z & \Omega_y \\ \Omega_z & 0 & -\Omega_x \\ -\Omega_y & -\Omega_x & 0 \end{bmatrix} = \Omega\begin{bmatrix} 0 & 0 & 1 \\ 0 & 0 & 0 \\ -1 & 0 & 0 \end{bmatrix} \tag{9}$$

Explicit definitions of these energies are given in more detail elsewhere [42].

Vibratory stress failure in the composite fan (Figs. 1 and 2) may originate from tensile and bending stresses partly due to the centrifugal force as a result of high rotational speeds and partly due to high pressure, temperature, and speed induced by the gas loading [43]. The potential due to centrifugal force was an essential consideration in the governing energy, especially given the arbitrary shape of the composite fan blades (Figs. 1 and 2). The present design synthesis aimed at reducing these tensile and gas bending stresses. One way the present design synthesis achieved this was by the balancing of blade mass through optimally reshaping the blade variable cross section (thickness) from the hub/dovetail to midradial height. The blade material was much more effectively utilized through this shape optimization. The loading on the composite fan was composed of centrifugal force due to rotation, bending force due to gas pressure and change of momentum, and bending force due to centrifugal ancillary effects, resulting from the centroids of all blade section not aligned along a single radial line (see Figs. 1 and 2).

The centrifugal tensile loading was peak at the blade hub/dovetail, decreasing towards the blade tip. The tensile stress (centrifugal stress) depends on the mass density of the composite angle-ply layup in the fan, blade radial height, fan rotational speed, and the volume of fan. The potential due to centrifugal body forces included in the proposed reduced-order spectral model was

$$W_\Omega = \{P_{CF}\}^T\Delta = \iiint \rho^{(p)}\{r + r_0\}^T[\Omega]\Delta dV \tag{10}$$

where $r = \{x,y,z\}^T$ indicated a position vector of bladed disk annulus coordinates, and r_0 a translational offset of these coordinates from the engine axis.

The gas bending stress peaks at the composite blade hub/dovetail. The combined tension and gas bending stress also peaks at composite blade hub/dovetail and diminishes with radius. As the composite fan blades were clearly tapered, the centrifugal tensile stress diminished rapidly towards the blade tips, while the gas bending stress increased albeit to lesser extent with increasing radial height. The centrifugal tensile stress is steady, whereas in actuality the gas flow-induced bending stress is quasi-steady as the fan blades pass through nonuniform flow distributions. The gas flow-induced bending stress is directly proportional to the blade height and fan stage work output (i.e., a product of the inlet mass flow and whirl velocity), and inversely proportional to the number of blades and the dovetail section modulus [43]. (The latter is a function of the blade camber and thickness-to-chord ratio). Moreover, the centrifugal bending stress can be highly sensitive to blade manufacturing imperfections and blade root fixing, and such centrifugal bending stress may cancel the gas flow-induced bending stress at the design wheel speed, especially as the schedule of blade radial sections is inclined relative to any radial line. In the present fan design synthesis, the schedule of fan blade centroids is assumed nearly radial. Hence, the centrifugal bending stress is negligible. Nonetheless, the potential due to gas flow bending forces,

$$W_G = \{P_G\}^T \Delta = \iiint \{\sigma_{gb}\}^T \Delta dV \tag{11}$$

with $\{\sigma_{gb}\}$ representing a gas bending stress vector, was assumed negligible in comparison to W_Ω, as the potential due to centrifugal body forces provided the most demanding influence on the total vibratory stress in the composite fan [43]. Provisions were made in the present design synthesis to optimize a composite fan that withstands the larger centrifugal tension stresses encountered in operation at a customary service life.

In using the Ritz variational procedure in the 3D ROME development, the total energy of the composite fan (Figs. 1 and 2) was constructed using the above Eqs. (1)–(11) as $\pi_p = U_L + U_\sigma - T_0 - T_\Omega - T_C - W_\Omega - W_G$.

3.2 Assumed Displacement Approximations. The temporal motion $\Delta = \{u,v,w\}^T$ of the composite fan was assumed to harmonically oscillate, as follows:

$$u(x,y,z,t) = \varphi_u(x,y,z)e^{\sqrt{-1}\omega t} \quad v(x,y,z,t) = \varphi_v(x,y,z)e^{\sqrt{-1}\omega t}$$
$$w(x,y,z,t) = \varphi_w(x,y,z)e^{\sqrt{-1}\omega t} \tag{12}$$

where ω represented the circular frequency of vibration and e is the exponential function. The displacement functions u,v,w were approximated as a mathematically complete set of modified Gram–Schmidt (MGS) orthogonal polynomials in x, y, z [38–40]:

$$\varphi_u(x,y,z) = \sum_{\alpha=1}^{\alpha} A_\alpha \Phi_\alpha(x,y,z) \quad \varphi_v(x,y,z) = \sum_{\beta=1}^{\beta} B_\beta \Phi_\beta(x,y,z)$$
$$\varphi_w(x,y,z) = \sum_{\eta=1}^{\eta} C_\eta \Phi_\eta(x,y,z) \tag{13}$$

In Eq. (13) the spatial displacements were approximated as a hybrid series consisting of what we defined as: (i) orthonormal "*blade*" polynomials—which captured the motion of the fan blades only attached to an assumed rigid mechanical element, such as a rigid disk, and (ii) orthonormal "*disk*" polynomials—which captured the motion of the composite fan, when the annulus was assumed rigidly clamped at the disk bore (thus, restricting all systemic rigid body motions) [1,2]. The assumed hybrid series of "*blade-disk*" polynomials is a generalized Fourier series. It is comprised of algebraic polynomials and boundary functions, which satisfy the essential kinematic boundary conditions satisfying assumed vanishing displacement conditions along the base of the dovetail of the cyclic symmetric composite fan system (Figs. 1 and 2). After the first term of the series was constructed as the simplest polynomials that satisfy the necessary kinematic boundary conditions, the subsequent higher terms of the series were generated using the MGS procedure. Thus, the assumed displacement fields of the composite fan annulus were mathematically complete [38–40] and a guaranteed upper bound convergence to an exact solution was obtained as a sufficient number of terms in the polynomial series were used.

Recursive formulae of Φ_k in Eq. (13) for $k = 1,2,3,\ldots,N$ was defined as

$$\Phi_k(x,y,z) = \frac{{}^{(i)}a_k(x,y,z)}{\int_v [{}^{(i)}a_k(x,y,z)]^2 dv} \tag{14}$$

where ${}^{(i)}a_k(x,y,z)$ is the kth generating polynomial term of the ith calculating step. At the first iteration, $i = 1$, the definition of the kth generating polynomial term was

$${}^{(1)}a_k(x,y,z) = \psi(x,y,z) \sum_{l=0}^{L} \sum_{m=0}^{l} \sum_{n=0}^{m} x^{l-m} y^{m-n} z^n \tag{15}$$

where ψ defined a boundary function such that all terms of Eq. (15) satisfied the assumed kinematics boundary conditions. L denoted the highest power of the polynomials, and l, m, n defined the associate integers for the polynomial terms set by L. Linking back to Eq. (13), let $\alpha = \beta = \eta = N$ indicate the total number of polynomial terms. The first MGS orthonormal polynomial term was

$$\Phi_1(x,y,z) = \frac{{}^{(1)}a_1(x,y,z)}{\int_v [{}^{(1)}a_1(x,y,z)]^2 dv} \tag{16}$$

For iterations $i = 2,3,\ldots,N$, every generating polynomial was updated according to the following recursive formulas:

$${}^{(i)}a_k(x,y,z) = {}^{(i-1)}a_k(x,y,z) - \Phi_{k-1}(x,y,z)\, r_{k-1,k}$$
$$r_{k-1,k} = \int_v \Phi_{k-1}(x,y,z)\, ({}^{(i-1)}a_k(x,y,z))\, dv \tag{17}$$

for $k = i,\ldots,N$. Equations (17) orthonormalize all of the generating polynomials of the ith step (i.e., ${}^{(i)}a_k(x,y,z)$) to the $(k-1)$th orthonormalized polynomial (i.e., $a_{k-1}(x,y,z)$). The kth orthonormal MGS polynomial term (i.e., $a_k(x,y,z)$) was obtained by normalizing the ${}^{(k)}a_k(x,y,z)$ by Eq. (14). For any polynomial a_k,

$$\int_v \Phi_k \Phi_k dv = 1 \quad \text{and} \quad \int_v \Phi_i \Phi_j dv = 0 \ (i \neq j) \tag{18}$$

The gradients of the displacement were needed to construct the engineering strains briefly outlined in Sec. 3.1. These strains were in turn used to calculate the deformational energy discussed in Sec. 3.1 leading to the stiffness of the composite fan. The first gradient of $a_k(x,y,z)$ with respect to the coordinates x,y,z was defined as

$$\Phi_{k,j}(x,y,z) = \frac{{}^{(i)}a_{k,j}(x,y,z)}{\int_v [{}^{(i)}a_k(x,y,z)]^2 dv} \tag{19}$$

where ${}^{(i)}a_{k,j}(x,y,z)$ indicated the first derivative of kth generating polynomial with respect to coordinate j (i.e., j being x, y and z). ${}^{(i)}a_k(x,y,z)$ was obtained from Eq. (17). For iteration $i = 1$,

$${}^{(1)}a_{k,j}(x,y,z) = \psi_{,j}(x,y,z) \left(\sum_{l=0}^{L} \sum_{m=0}^{l} \sum_{n=0}^{m} x^{l-m} y^{m-n} z^n \right)$$
$$+ \psi(x,y,z) \left(\sum_{l=0}^{L} \sum_{m=0}^{l} \sum_{n=0}^{m} x^{l-m} y^{m-n} z^n \right)_{,j} \tag{20}$$

For iterations $i = 2,3,\ldots,N$, the first derivative of subsequent generating polynomials was calculated using the following recursive formulas:

$${}^{(i)}a_{k,j}(x,y,z) = {}^{(i-1)}a_{k,j}(x,y,z) - \Phi_{(k-1),j}(x,y,z)\, r_{k-1,k} \tag{21}$$

for $k = i,\ldots,N$, and where r_{k-1} was obtained from Eq. (17).

3.2.1 Generating Functions for Composite Fan Polynomials. For an assumed cyclic symmetric (isolated composite fan blade) analysis (Figs. 1 and 2), the assumed boundary conditions were the essential kinematic boundary conditions satisfying assumed vanishing displacement conditions along the base of the dovetail

and completely free at all other edges. Accordingly, the kth generating polynomial of the first calculating step was

$$^{(1)}a_k(x,y,z) = \psi_b(x,y,z)\left(\sum_{l=0}^{L}\sum_{m=0}^{l}\sum_{n=0}^{m} x^{l-m}y^{m-n}z^{n}\right) \tag{22}$$

where $\psi_b(x,y,z)$ was a function that satisfied the essential conditions of vanishing displacements at the blade root.

For an integrated composite bladed disk analysis [1,2], the dynamics consist of the elastic motion of the blades only attached to an assumed rigid disk, and the flexible disk-induced motion of the entire composite fan. To capture these motions, two types of generating functions with associated boundary functions were used. First, the kth *disk* polynomials of the first calculating step for approximating the disk-induced motions were as follows:

$$^{(1)}a_k(x,y,z) = \psi_d(x,y,z)\left(\sum_{l=0}^{L}\sum_{m=0}^{l}\sum_{n=0}^{m} x^{l-m}y^{m-n}z^{n}\right) \tag{23}$$

where $\psi_d(x,y,z)$ was a disk boundary function satisfying vanishing displacements at the disk bore to restrict the annulus from rigid body motions. Second, the kth *blade* polynomials of the first calculating step for approximating the blade-only motions were as follows:

$$^{(1)}a_k(x,y,z) = \psi_b(x,y,z)\left(\sum_{l=0}^{L}\sum_{m=0}^{l}\sum_{n=0}^{m} x^{l-m}y^{m-n}z^{n}\right) \tag{24}$$

where $\psi_b(x,y,z)$ was a blade-only boundary function satisfying vanishing displacements at the blade root (all other edges completely free). As typically used in component-mode methods, it was undesirable to assume the blade-only elastic motions as completely unrestrained. This is because the blades generally vibrate as clamped-free rather than free-free components around the composite fan. In addition, a larger number of the free-free blade polynomials would be needed to sufficiently model the blade responses around the disk. The generating polynomials of the first calculating step combine the blade-disk polynomials (Eqs. (23) and (24)) [1,2]:

$$^{(1)}a(x,y,z) = \underbrace{^{(1)}a_1,\ ^{(1)}a_2,\ ^{(1)}a_3,\ \ldots,\ ^{(1)}a_{K_d}}_{\boxed{\text{Fan Dovetail Eq. (24)}}} \times \underbrace{^{(1)}a_{K_{d+1}},\ ^{(1)}a_{K_{d+2}},\ ^{(1)}a_{K_{d+3}},\ldots,\ ^{(1)}a_{K_d+K_b}}_{\boxed{\text{Fan Blade Eq. (25)}}} \tag{25}$$

where $N = K_d + K_b$ were the total number of terms incorporating the total number of disk polynomials (K_d) and total number of blade polynomials across all blades of the system (K_b).

After obtaining the first step's generating polynomials either for an assumed cyclic symmetric (isolated composite fan blade) analysis (Figs. 1 and 2) or for an entire composite fan assembly, the MGS orthonormal polynomials were calculated using the procedures described in the previous section by substituting the generating polynomials (Eqs. (22) or (24)) into Eqs. (14)–(18). The spatial derivatives of the MGS polynomials were obtained from Eqs. (19)–(21).

3.3 Numerical Integration Procedures. In order to numerically evaluate the required integrals of the dynamical energies discussed in Sec. 3.1, and the assumed displacement MGS polynomial approximations (Eqs. (12)–(25)), integration points were mapped over the composite fan's assumed cyclic symmetric domain in Cartesian (x,y,z) space (see Figs. 1 and 2). The energy functionals, symbolically represented here as $f(x,y,z)$ were evaluated. Hence, an accurate value of integration was numerically achieved using a simple trapezoidal rule, as a reasonably sufficient number of points were utilized. This is symbolically represented in the following triplicate summation of the energy functional $f(x,y,z)$ evaluated across the total number of integration points ($i=b, j=c, k=d$) over the composite fan's assumed cyclic symmetric domain:

$$\int_{x_1(x)}^{x_2(x)}\int_{y_1(x,y)}^{y_2(x,y)}\int_{z_1(x,y,z)}^{z_2(x,y,z)} f(x,y,z)\,dz\,dy\,dx = \sum_{i=1}^{i=b}\sum_{j=1}^{j=c}\sum_{k=1}^{k=d} f(x_i,y_j,z_k)\Delta z\Delta y\Delta x \tag{26}$$

3.4 Synthesis of 3D ROME Equations for Free Response of a Composite Fan. Substituting Eqs. (12)–(17) into the energy functions given in Sec. 3.1 and setting the exponential terms to unity in Eqs. (12), one obtains the maximum total energy $(\pi_p)_{\max} = (U_L + U_\sigma - T_0 - T_\Omega - T_C - W_\Omega - W_G)_{\max}$. This resulting maximum total energy $(\pi_p)_{\max}$ is minimized with respect to the generalized coefficients $\{q\} = \{A_\alpha, B_\beta, C_\eta\}$ of the displacement trial functions (Eqs. (13)), resulting in $\partial(\pi_p)_{\max}/\partial A_\alpha, = 0; \partial(\pi_p)_{\max}/\partial B_\beta, = 0; \partial(\pi_p)_{\max}/\partial C_\eta, = 0$. If no kinematic constraints other than the vanishing kinematics at the base of the hub of the composite blade were imposed (Figs. 1 and 2), and no other admissible terms up to L were omitted, then the set of polynomial terms in Eqs. (15) were characterized mathematically complete [38–40]. With a sufficient number of terms of the assumed in the displacement trial functions (Eqs. (15)), the calculated frequencies should in principle converge monotonically from above to exact values, where the formal solution of the governing partial differential equations of motion is intractable through simple separable variables for an arbitrarily shaped composite bypass fan (Fig. 1).

The Ritz minimization resulted in a set of nonlinear algebraic equations, which were iteratively solved for $\{q\}$. The resultant nonlinear equations of motion constructed and solved are symbolized as

$$[K_L + K_{CF} + K_{NL}(q)]\{q\} + [C]\{\dot{q}\} + [M]\{\ddot{q}\} = \{P_{CF}\} + \{P_G\} \tag{27}$$

where $[K_L + K_{CF} + K_{NL}(q)]$ denoted the linear, centrifugal, and geometrically nonlinear stiffness contributions, $[C]$ is the dissipative-gyroscopic matrix (included because a small amount of viscous mechanical damping was assumed in the composite fan analysis), $[M]$ is the mass matrix, $\{P_{CF}\}$ is the steady-state centrifugal tension, and $\{P_G\}$ is the steady-state gas bending load, which is assumed negligible in the present analysis compared to $\{P_{CF}\}$. Explicit definitions of these structural matrices and vectors are given elsewhere [42]. Equation (27) was solved in two steps: first, using a Newton–Raphson iterative solution procedure, the geometrically nonlinear static equilibrated position $\{q_s\}$ of the bladed disk due to the centrifugal load $\{P_{CF}\}$, and assumed negligible $\{P_G\}$ compared to $\{P_{CF}\}$, was determined,

$$[K_L + K_{CF} + K_{NL}(q)]\{q_s\} = \{P_{CF}\} + \{P_G\} \tag{28}$$

and second, the bladed disk was subjected to a linear temporal perturbation $\{q_p(t)\}$ about the static geometrically nonlinear displaced position $\{q_s\}$, as follows:

$$[K_T]\{q_p\} + [C]\{\dot{q}_p\} + [M]\{\ddot{q}_p\} = \{0\} \tag{29}$$

where the tangential stiffness $[K_T]$ was defined as

$$[K_T] = \left[K_L + K_{CF} + K_{NL}(q_s) + \frac{\partial K_{NL}(q_s)}{\partial q}\right] \tag{30}$$

Assuming $\{\chi\} = \{\dot{q}_p, q_p\}^T = \{\Xi\}e^{\gamma t} = \{\Xi\}e^{(\sqrt{-1}\omega - \xi)t}$, a first-order eigenvalue problem was obtained:

$$[[A] - \gamma[B]]\{\Xi\} = [[A] - (\sqrt{-1}\omega - \xi)[B]]\{\Xi\} = \{0\} \quad (31)$$

where $[A]$ is symmetric and $[B]$ is antisymmetric:

$$[A] = \begin{bmatrix} [M] & [0] \\ [0] & [K_T] \end{bmatrix}, \quad [B] = \begin{bmatrix} [0] & [M] \\ -[M] & -[C] \end{bmatrix} \quad (32)$$

and γ is a complex eigenvalue; the real part representing exponential variations (of decay rate $= \varpi$) and the imaginary part as the harmonic component (at circular frequency ω). Eigenvectors $\{\Xi\}$ involving the coefficients $\{q\} = \{A_{\alpha i}, B_{\beta i}, C_{\eta i}\}$ may be determined in the usual manner by substituting the eigenvalues back into the homogeneous Eqs. (31) and (32). Normalized contours of the associated mode shapes may be depicted on any arbitrary 3D grid over the composite fan domain once the eigenvectors $\{\Xi\}$ are substituted into Eqs. (12)–(15). Mechanical stresses of the composite fan were characterized maximum at the dovetail base and were obtained once the modal displacements (Eqs. (12)–(15)) were backsubstituted into the energy functions outlined in Sec. 3.1.

It should be noted that a uniform grid of nodal point locations was typically employed in the present analysis, yielding the depiction of the composite fan shown in Fig. 1. The number of nodes needed was determined by one less than the maximum degree order L of polynomial approximation utilized for the assumed bladed-disk functions (Eqs. (12)–(15), (25)). We acknowledge that industry practice suggests nodal point location can be particularly important in cyclically symmetric structures. If the node locations are not cyclically symmetric, then the elastic and inertial energies are not cyclically symmetric, i.e., the system is numerically mistuned. Although this effect is small, it is well known that the composite fan was sensitive to small angle-ply laminate construction misalignments [44–48], so that this effect of numerical mistuning is sometimes unavoidable unfortunately.

The present model [1,2] described above is a considerable improvement of previous work [42]. It is simple and efficient to use for the extremely large number of fan reanalyses required for the sensitivity analyses essential to nonlinear design optimization of bypass engine fans. Essential design sensitivities of constraints are cost effective to monitor, as a number of fan configuration parameters are changed, namely aspect ratio (a/b), chord ratio (c/b), percent thickness (t_h/b), dovetail-to-casing ratio ($a_H/(a_T)$, stagger angle φ_o, dovetail slope β_H, angular velocity (Ω), ply-orientation angle (θ), laminate stacking arrangements and orthotropic material properties, blade profile shape, etc.

4 Geometry and Material Properties of Baseline Fan

Shown in Table 1 are the geometric properties of the baseline fan design. Additional geometrical definitions include: dovetail slope angle $\beta_H = 12.5$ deg; dovetail-to-casing ratio $a_H/a_T = 0.3$; blade height $a = (a_T - a_H) = 43$ in. (1.0922 m); root height $a_R = 13.5$ in. (0.3429 m) dovetail chord $b_R = 5$ in. (0.127 m) supersonic relative velocity @ blade tip $V_\infty = 1452.1$ (ft/s) (442.9 (m/s)); relative Mach number @ blade tip $M_T = (V_\infty/a_\infty) = 1.3$ ($a_\infty = 1117$ (ft/s) (340.7 (m/s))); blade tip speed $V_T = 1341$ (ft/s) (409 (m/s)); fan solidity $\sigma \approx 1$; design wheel speed $\Omega = V_T/a_T = 261.79$ (rad/s) $= 2500$ rpm $= 41.67$ Hz; and frequency ratio $\Omega/\omega_o = 1.5$, where ω_o is the fundamental (lowest) frequency of the tuned stationary fan.

Table 1 Geometric properties of baseline composite bypass fan

	Dovetail	Mean	Tip
a in (m)	$a_H = 18.5$ (0.4699)	35 (0.889)	$a_T = 61.5$ (1.5621)
b in (m)	$b_H = 12$ (0.3048)	16.75 (0.4255)	$b_T = 21.5$ (0.5461)
t_H/b	15%	7%	2%
Twist ϕ_x	+4.4 deg	−34.4 deg	−59.6 deg
Dovetail	$\beta_H = 12.5$ deg	–	–

A 3D curve fit of a NACA 65-series profile has been used to approximate the suction $Z_s(x,y)$ and pressure $Z_p(x,y)$ surfaces and the camber line $\gamma(x,y)$ of the baseline fan blades (Fig. 2):

$$Z_s(x,y) = a_0 + a_1\xi + a_2\xi^2 + a_3\xi^3 + a_4\xi^4 + a_5\xi^5 + a_6\xi^6 \quad (33)$$

$$Z_p(x,y) = a_0 + a_1\xi + a_2\xi^2 + a_3\xi^3 + a_4\xi^4 + a_5\xi^5 + a_6\xi^6 \quad (34)$$

$$\gamma(x,y) = a_0 + a_1\xi + a_2\xi^2 + a_3\xi^3 + a_4\xi^4 + a_5\xi^5 + a_6\xi^6 \quad (35)$$

where the coefficients in the above equations are charted below

	a_0	a_1	a_2	a_3	a_4	a_5	a_6	Eq.
$Z_s(x,y) =$	0.84	$5.0(10^{-2})$	$-5.9(10^{-2})$	$1.2(10^{-3})$	$1.0(10^{-3})$	$-7.8(10^{-5})$	$-2.6(10^{-5})$	(33)
$Z_p(x,y) =$	−1.1	$-5.9(10^{-2})$	$9.6(10^{-3})$	$-1.1(10^{-3})$	$-5.3(10^{-4})$	$7.0(10^{-5})$	$4.0(10^{-6})$	(34)
$\gamma(x,y) =$	−0.1	−0.0043	$-2.5(10^{-2})$	$4.7(10^{-5})$	$2.4(10^{-4})$	$-4.1(10^{-6})$	$-1.1(10^{-5})$	(35)

and

$$\xi = t_h(x) \times y[0.6594 + 0.01841x]^{-1} \quad (36)$$

The thickness distribution $t_h(x)$ of the fan blades from dovetail to tip (Fig. 3) is assumed as follows:

$$t_h(x) = 1 + m_T[(x - x_0)/L_{\text{blade}}] - 2(0.95 + m_T)[(x - x_0)/L_{\text{blade}}]^2 + (1.1 + m_T)[(x - x_0)/L_{\text{blade}}]^3 \quad (37)$$

where $x_0 = a_R = 13.5$ in. (0.3429 m) is the root radius, $L_{\text{blade}} = a = (a_T - a_H) = 43$ in. (1.0922 m) is the radial height of the blade, and m_T is a tuning variable used for the fan mass-balancing (shape) optimization, which determines the slope (angle in degrees) of the thickness distribution of the fan blades relative to the dovetail thickness to the thickness at approximately the mean radial height (see Fig. 3). Tuning the fan thickness in this fashion is consistent with common practice of metallic titanium fan vibration control used by industry designers.

All volumetric integrals, shown in [1], were numerically evaluated within the blade profile surfaces Z_s and Z_p. Using velocity triangles, the incidence angle was defined as $\theta_I = (V_x/V_\theta)$, where the assumed axial flow velocity was half the blade tip Mach number $V_x = 0.5M_T$, and the tangential flow velocity $V_\theta = \Omega_r$. Additional angle of flow incidence causes the torsional motion itself to either dissipate out or supplement in composite fan flexure. Thus, the radial distribution of fan pretwist is assumed averaged such that the angle of incidence along the radial height of the bypass fan is zero consistent with common practice of fan vibration control used by industry designers. The camber line $\gamma(x,y)$ of the

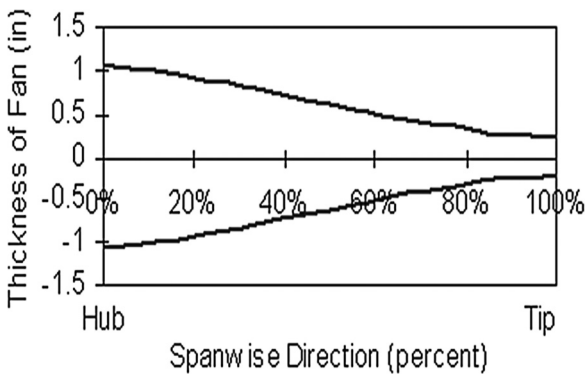

Fig. 3 Dovetail (hub)-to-tip thickness distribution of the baseline composite bypass fan

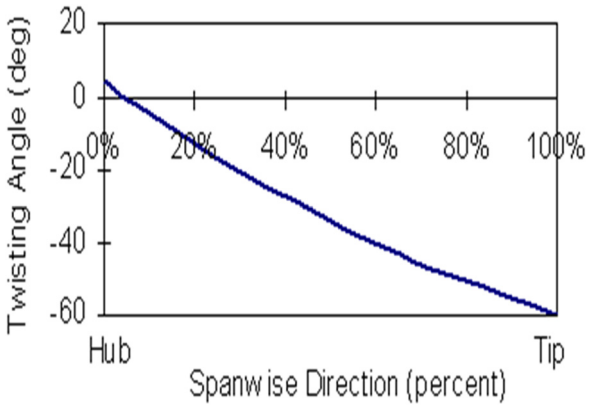

Fig. 4 Dovetail (hub)-to-tip pretwist angle variation of the baseline composite bypass fan

airfoil also changed the incidence angle. Hence, the fan blades were assumed pretwisted accordingly as $\phi_x(x) = \gamma(x,y) - \theta_I$, (charted in Fig. 4), to ensure zero incidence $\theta_I = (V_x/V_\theta) = 0$ deg from dovetail to tip:

$$\phi_x(x) = f(x)/g(x) - 57.30\ \tan^{-1}(0.039x) \tag{38}$$

$$f(x) = (35.87)[37.89 + x][1364.61 + 73.88x + x^2] \times [1418.07 + 75.09x + x^2] \times [1.12 - (1.09 \times 10^{-4})x - (5.10 \times 10^{-4})x^2 + (4.36 \times 10^{-6})x^3] \tag{39}$$

$$g(x) = (35.82 + x)^5 \tag{40}$$

A graphite-epoxy (AS-4/3501–6) material [49,50] having strong orthotropy was assumed for the angle-ply lamination properties of the baseline fan: elastic constants $E_{11} = E_L = 21.044(10^6)$ psi (144.993 GPa), $E_{22} = E_{33} = E_T = 1.538(10^6)$ psi (10.596 GPa); shear constants $G_{12} = E_{11}/2(1-\nu_{12})$, $G_{21} = E_{22}/2(1-\nu_{21})$, $G_{23} = E_{22}/2(1-\nu_{23})$, $G_{32} = E_{33}/2(1-\nu_{32})$, $G_{13} = E_{11}/2(1-\nu_{13})$, $G_{31} = E_{33}/2(1-\nu_{31})$, noting $G_{LT} = 1.103(10^6)$ psi (7.599 GPa); Poisson's ratio relations, $\nu_{12}E_{11} = \nu_{21}E_{22}$, $\nu_{23}E_{22} = \nu_{32}E_{33}$, $\nu_{13}E_{11} = \nu_{31}E_{33}$, noting $\nu_{LT} = 0.27$; material density $\rho^{(p)} = 55(10^{-3})$ (lb/in.^{3}) $= 0.1423(10^{-3})$ (slug/in.^{3}). For graphite-epoxy material $\sigma_{LU} = 303(10^3)$ psi (2.09 GPa) and $\sigma_{TU} = 9.28(10^3)$ psi (0.064 GPa), when the principal fiber stresses σ_x and σ_y were tensile in the constraint Eq. (28), and $\sigma_{LU} = 208(10^3)$ psi (1.44 GPa) and $\sigma_{TU} = 33.06(10^3)$ psi (0.228 GPa), when σ_x and σ_y were compressive in Eq. (60), and $\sigma_{LTU} = 10.29(10^3)$ psi (0.071 GPa).

Symmetric placement of the angle plies θ_i $(i = 1,2,\ldots,N_{\text{plies}})$ about the middle plane of the baseline fan blades were assumed, as a sufficient restriction of certain combinations of in-plane and bending stiffness effects [13–15,41,51]. The laminate designs consist of two symmetric sublaminates with equal numbers of plies and equal but arbitrary angle-ply orientations θ_i for which the minimum number of plies is eight.

5 Mechanical Response of Baseline Fan

The baseline fan frequency and mode shape calculations summarized here were performed on an IBM/RS-6000 970 power server with an IBM/RS-6000 340 workstation cluster using double precision (14 significant-digit) arithmetic and a Dec3000 Alpha Station 500/266. The associated eigenvalue problem was positive definite, and thus the fan frequencies and mode shapes were obtained by using a QL algorithm combined with a Cholesky factorization [52–54].

Consider the baseline fan design (Figs. 1–4) having a symmetric eight-ply orientation of [0 deg, +45 deg, 0 deg, −45 deg]$_s$ with ply thicknesses 0.098 in. (0.249 cm), 0.098 in. (0.249 cm), 0.196 in. (0.498 cm), and 0.49 in. (1.245 cm), respectively. The ply orientations were assumed to be designed for principal shear stress resistance to torsional deformation, and for principal normal stress resistance to centrifugal tension. The thicknesses were setup to create a baseline fan with frequencies in specific ranges for

Table 2 3D ROME cyclic frequencies (Hz)[a] of stationary 8-ply baseline composite bypass fan ([0 deg, +45 deg, 0 deg, −45 deg]$_s$ ply-orientation of 0.098 in. (0.249 cm), 0.098 in. (0.249 cm), 0.196 in. (0.498 cm), and 0.49 in. (1.245 cm) ply-thicknesses, respectively)

Terms	500[b]	525	550	575	600	625	650	650[c]	ANSYS[d] 40 × 60 × 8
DOF	1500	1575	1650	1725	1800	1875	1950	1950	45,264
1B	28.78	28.78	28.78	28.75	28.73	28.73	28.73	28.68	29.6
2B	61.23	61.21	61.20	61.11	61.05	61.02	61.01	60.78	63.1
1T	136.8	136.8	136.8	136.7	136.7	136.7	136.6	136.0	142.9
3B	142.8	142.8	142.8	142.6	142.5	142.4	142.4	142.1	149.0
5M	214.3	214.1	214.1	213.6	213.3	213.1	213.1	211.4	208.1
6	259.7	259.6	259.5	259.3	259.2	259.2	259.1	258.9	260.9
7	311.5	311.5	311.5	311.1	310.9	310.8	310.8	310.2	314.9
8	358.3	358.0	357.8	356.9	356.7	356.6	356.5	356.1	376.5
9	423.5	423.3	423.1	422.6	422.5	422.4	422.3	422.1	441.3
10	462.3	461.9	461.6	459.7	459.2	459.1	458.9	458.3	459.8
11	494.2	493.7	493.3	492.6	492.2	492.0	491.8	490.8	523.9
12	578.4	577.5	576.6	575.6	574.2	573.7	573.3	572.8	594.2
13	599.7	598.7	597.6	590.7	588.0	587.6	587.0	586.9	627.1
14	630.5	629.5	629.2	623.8	622.6	622.5	622.3	622.2	683.4
15	695.9	695.6	695.4	680.6	680.1	679.9	679.8	678.3	692.4
16	762.1	761.3	760.7	753.9	744.1	742.5	741.7	739.6	811.3
17	830.8	829.7	828.5	815.2	802.5	800.7	799.8	798.0	825.9
***[e]	226.2	226.0	226.0	225.9	225.8	225.8	225.7	225.7	743.7
****	371.9	371.6	371.5	371.2	371.0	370.9	370.8	370.7	881.3
****	640.8	639.8	639.0	637.9	637.5	637.2	636.8	636.0	907.0

[a]Design wheel speed $\Omega = V_T/a_T = 0$.
[b]Total number of 3D ROME polynomials terms, for instance, a 500-term solution indicates that $\alpha = \beta = \eta =$ 500 orthonormal polynomial terms (Eqs. (14)–(17), (22)–(25)) were retained in each of the blade height (u), chord (v), and thickness (w) displacement trial functions, resulting in a solution matrix determinant size of 1500 degrees of freedom.
[c]Lower-bound imperfectly restrained 3D ROME solutions.
[d]ANSYS FEM grid size, $l \times m \times n$, l = SOLID8 in blade height, m = SOLID8 along chord, n = SOLID8 in thickness.
[e]**** Extra modes.

Table 3 3D ROME cyclic frequencies (Hz)[a] of rotating 8-ply baseline fan ([0 deg, +45 deg, 0 deg, −45 deg]$_s$ ply-orientation of 0.098 in. (0.249 cm), 0.098 in. (0.249 cm), 0.196 in. (0.498 cm), and 0.49 in. (1.245 cm) ply-thicknesses, respectively)

Terms	500[b]	525	550	575	600	625	650	650[c]	ANSYS[d] $40 \times 60 \times 8$
DOF	1500	1575	1650	1725	1800	1875	1950	1950	45,264
1B	52.01	52.00	51.99	51.93	51.89	51.87	51.87	51.69	52.5
2B	103.7	103.7	103.7	103.6	103.5	103.5	103.5	103.2	102.9
1T	146.1	146.1	146.1	146.0	145.9	145.9	145.9	145.7	153.5
3B	193.8	193.7	193.6	193.4	193.2	193.1	193.1	191.8	190.6
5M	254.4	254.3	254.2	253.9	253.7	253.6	253.6	252.8	248.4
6	283.1	282.9	282.9	282.7	282.6	282.6	282.6	282.3	269.2
7	373.5	373.5	373.2	373.0	372.9	372.8	373.0	372.8	354.3
8	389.8	389.4	389.0	388.1	388.0	388.2	388.5	387.7	389.4
9	444.6	444.6	444.2	444.0	443.7	443.4	443.2	443.2	430.9
10	495.7	495.7	494.4	489.3	488.8	487.5	486.1	486.1	476.2
11	540.8	540.5	540.3	539.1	538.8	538.7	538.5	537.2	540.4
12	568.3	567.3	566.0	565.9	563.4	563.6	563.4	563.0	573.0
13	605.0	603.4	604.6	593.4	591.6	591.0	586.8	586.6	604.3
14	658.2	657.6	656.4	654.5	654.9	654.2	653.5	653.0	665.9
15	676.0	675.4	675.3	672.7	672.0	671.0	668.6	667.8	704.1
16	739.5	739.3	738.9	728.7	727.7	727.0	726.5	725.4	743.1
17	775.3	775.1	774.5	766.1	757.4	754.7	751.9	749.2	779.7
****[e]	848.1	847.0	844.5	833.7	821.1	818.5	815.3	813.8	821.6
*****	227.9	227.8	227.6	227.6	227.3	227.2	227.2	227.1	872.1
*****	342.0	341.8	340.8	340.2	339.7	339.2	339.1	339.0	900.8

[a]Design wheel speed $\Omega = V_T/a_T = 261.79$ (rad/s) $= 2500$ rpm $= 41.67$ Hz; frequency ratio $\Omega/\omega_o = 1.5$; ω_o is the fundamental (lowest) frequency of the stationary blade.
[b]Total number of 3D ROME polynomials terms, for instance, a 500-term solution indicates that $\alpha = \beta = \eta = 500$ orthonormal polynomial terms (Eqs. (14)–(17), (22)–(25)) were retained in each of the blade height (u), chord (v), and thickness (w) displacement trial functions, resulting in a solution matrix determinant size of 1500 degrees of freedom.
[c]Lower-bound imperfectly restrained 3D ROME solutions.
[d]ANSYS FEM grid size, $l \times m \times n$, $l =$ SOLID8 in blade height, $m =$ SOLID8 along chord, $n =$ SOLID8 in thickness.
[e]**** Extra modes.

demonstration purposes of the present reduced-order spectral-based (ROS) design synthesis technology discussed in more detail in Sec. 7.2. Using the 3D ROME analysis described in previous work [1,2], it was appropriate to ascertain how many terms of the assumed displacement polynomials were required to yield reasonably accurate vibration solutions of the baseline fan. Although significantly important in 3D vibration models of monolithically metallic fans, shear deformation and rotary inertia effects are typically much more important for the vibration of laminated composite fans, especially when the ply layers are strongly orthotropic (e.g., boron or graphite fibers in epoxy resin). Thus, for such materials, it is essential that no unnecessary kinematic restrictions are imposed upon the assumed 3D displacement fields, as in the present reduced-order analysis. Most of all, the present analysis is useful for cost-effective calculations of fan mechanical response during numerous iterative redesign cycles required of modern design synthesis techniques and general-purpose nonlinear mathematical optimization software packages.

Tables 2 and 3 summarize a brief convergence study of the first ten cyclic frequencies of the stationary and rotating baseline composite fans (excluding the effects of steady gas flow-induced loads, i.e., $P_G = 0$). Convergence of frequencies is shown in Tables 2 and 3, as the total number of polynomial terms (Eqs. (14)–(17), (22)–(25)) was increased from a 500-term solution to a 650-term solution [1,2]. A 650-term solution indicates that $\alpha = \beta = \eta = 650$ orthonormal polynomial terms (Eqs. (14)–(17), (22)–(25)) were retained in each of the blade height (u), chord (v), and thickness (w) displacement trial functions, resulting in a solution matrix determinant size of only 1950 degrees of freedom (DOF) (as indicated in Tables 2 and 3). One can see clearly in Fig. 5 that a good monotonic convergence of solution for at least the first 20 frequency modes was achieved using the present 3D reduced-order vibration analysis. For the first 20 modes, the average percentage difference between the 625-term and 650-term solutions was approximately 0.1%. By retaining additional terms in the displacement polynomials, one can, in principle, achieve better convergence of solution. In the fan design synthesis, which is discussed later, we focused on controlling the separation margins between the lowest three cycle frequencies on the Campbell diagrams [4] of the baseline fans.

To make the baseline composite fan design synthesis more efficient, the present calculations employed a computationally cheaper 100-term solution instead of the more expensive fully converged 650-term solutions, listed in Tables 2 and 3. Although not shown in Tables 2 and 3, the convergence studies revealed that for the first three modes restructured on the Campbell diagram for vibration control and integrally employed in the fan design synthesis, the percentage difference between the 100-term (300 DOF) and 650-term (1950 DOF) ROME free response solutions was approximately 1%, sufficient for engineering accuracy of the numerous reanalyses required in the computational reduced-order design synthesis outlined later.

5.1 Estimates of 3D ROME Solution Error. In theory and practice it is essential to provide estimates for solution error of the present 3D ROME predictions [1]. As can be seen in this work in Tables 2 and 3 the present 3D ROME method always leads to upper bounds on the exact solutions. Only the detailed convergence studies in each of Tables 2 and 3 alongside the percentage difference between the present 3D ROME solutions and the general-purpose ANSYS FEM results, shown in Tables 2 and 3, allows one to infer the upper-bound convergence accuracy of the present 3D solutions. Such inference does not, however, allow one to estimate the error of the present 3D solutions, and thus, the logical reasoning of the accuracy of the present 3D ROME method must be regarded as incomplete in theory through just a convergence study of cyclic frequencies.

Nonetheless, there is an easily implemented classical approach based on the inherent upper-bound convergence property of the present 3D ROME method, which we employed to theoretically estimate lower bounds on the exact solutions of the baseline

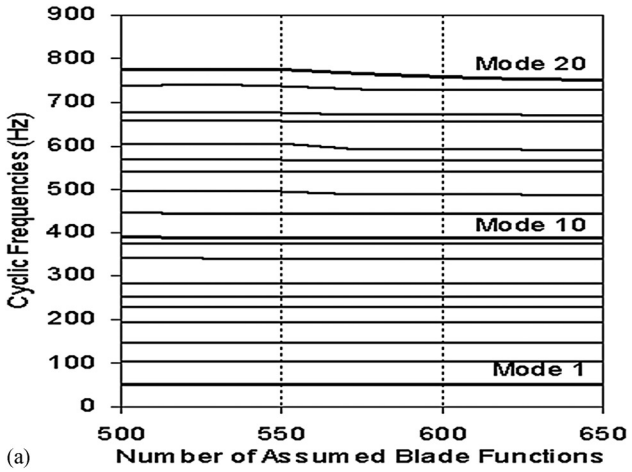

$$\frac{u}{a+u} = \frac{0.25\%\, d}{d} \quad \Rightarrow \quad u = \frac{0.25\%\, a}{(1-0.25\%)}$$

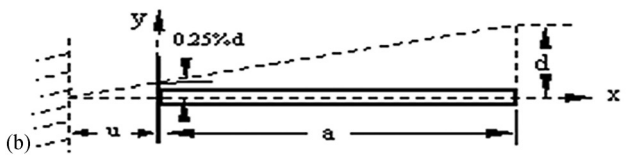

Fig. 5 Convergence of cyclic frequencies of rotating baseline composite bypass fan ([0 deg, +45 deg, 0 deg, −45 deg]$_s$ ply-orientation of 0.098 in. (0.249 cm), 0.098 in. (0.249 cm), 0.196 in. (0.498 cm), and 0.49 in. (1.245 cm) ply-thicknesses, respectively). (*a*) Imperfectly restrained boundary conditions.

composite fan cyclic frequencies of Tables 2 and 3. Here, lower bounds on the exact solutions were obtained by releasing the 3D restrained boundary conditions of the baseline fan blade-disk interface (Figs. 1 and 2), as geometrically interpreted and depicted in Fig. 5(*a*), and by allowing a restraint release ratio of 0.25% relative to the fan blade tip. Such results are hereafter described as the present *lower-bound imperfectly restrained 3D solutions*. The imperfect restraint was invoked by slightly shifting the restraint from $(x = 0)$ to $(x = -u)$ and allowing a prescribed displacement at the fan blade-disk root section at a ratio of 0.25% of the displacement (d) at the fan blade tip.

As previously stated, a strong upper-bound convergence of the perfectly restrained 3D solutions is shown in Tables 2 and 3, where the predicted difference between the 625-term and 650-term perfectly restrained 3D solutions averaged less than 0.1% over all 20 modes shown therein. Tables 2 and 3 also indicate that lower bound 650-term imperfectly restrained 3D solutions are only negligibly lower than the 650-term perfectly restrained 3D solutions by less than approximately 1% on average. This allows one to estimate the error of the present 3D ROME solutions in Tables 2 and 3 to be well below 1%. Thus, the convergence accuracy and solution error of the present 3D ROME method can be regarded as estimated, both completely and theoretically, in that the exact solution to the baseline composite fan vibrations must lie well inside a 1% bandwidth between the converged perfectly restrained upper-bound and imperfectly restrained lower, upper-bound 3D solutions, shown in Tables 2 and 3.

5.2 Comparison of 3D ROME and Finite Element Baseline Fan Vibrations. Figure 6 compares cyclic frequencies of the rotating baseline composite fan (at design wheel speed $\Omega = V_T/a_T = 261.79$ (rad/s) $= 2500$ rpm $= 41.67$ Hz; and frequency ratio $\Omega/\omega_o = 1.5$, where ω_o was the fundamental (lowest) frequency of the tuned stationary fan) obtained using the widely distributed ANSYS (Version 5.0a) general-purpose finite element software package. Very good agreements can be seen with 5% difference for the first ten modes. The ANSYS finite element discretization of the baseline composite fan shown in Fig. 7 consists of 15,088 nodes (with three translational DOF/node) connecting 19,200 eight-node SOLID46 composite elements (that is, a $l \times m \times n = 40 \times 60 \times 8$ grid, where l,m,n denotes the number of solid elements used along the blade height, chord, and thickness directions). All nodal displacements along the base of the dovetail were constrained. Table 4 shows a small sequential level of convergence of finite element solutions in that the $40 \times 60 \times 8$ grid contains the $40 \times 20 \times 8$ grid, which contains the $20 \times 10 \times 8$ grid.

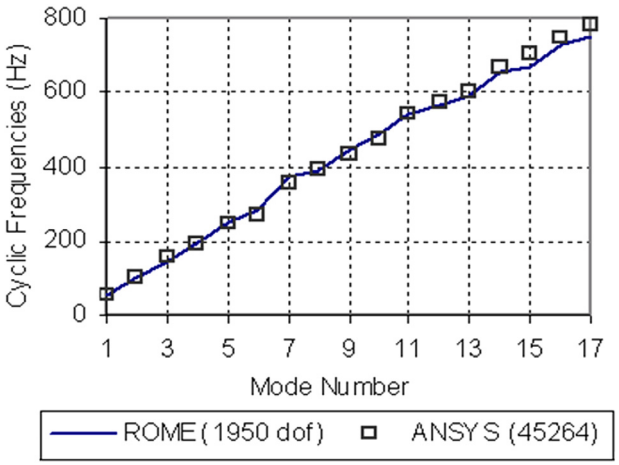

Fig. 6 Comparison of cyclic frequency accuracy of rotating baseline composite bypass fan ([0 deg, +45 deg, 0 deg, −45 deg]$_s$ ply-orientation of 0.098 in. (0.249 cm), 0.098 in. (0.249 cm), 0.196 in. (0.498 cm), and 0.49 in. (1.245 cm) ply-thicknesses, respectively)

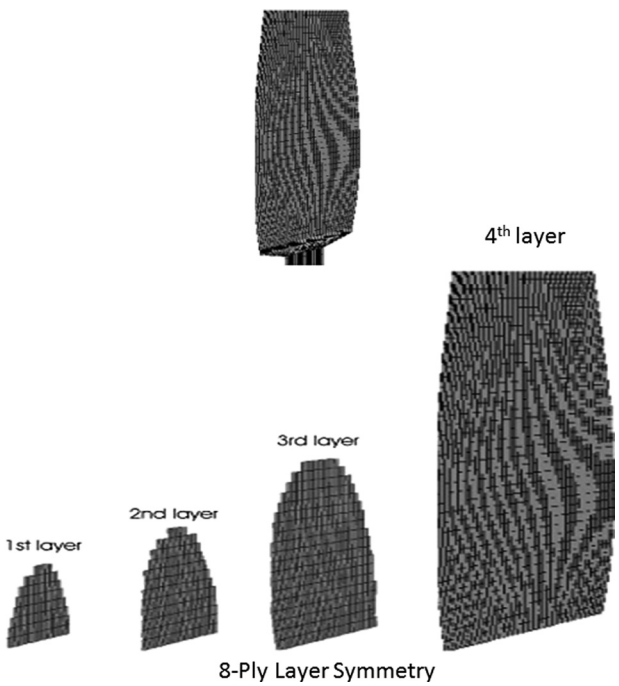

Fig. 7 Typical ANSYS finite element analysis discretization ($40 \times 60 \times 8$ grid shown) of an 8-ply baseline composite bypass fan ([0 deg, +45 deg, 0 deg, −45 deg]$_s$ ply-orientation of 0.098 in. (0.249 cm), 0.098 in. (0.249 cm), 0.196 in. (0.498 cm), and 0.49 in. (1.245 cm) ply-thicknesses, respectively)

Table 4 ANSYS FEM cyclic frequencies (Hz)[a] for the rotating[b] 8-ply baseline composite bypass fan ([0 deg, +45 deg, 0 deg, −45 deg]$_s$ ply-orientation of 0.098 in. (0.249 cm), 0.098 in. (0.249 cm), 0.196 in. (0.498 cm) and 0.49 in. (1.245 cm) ply-thicknesses, respectively)

Mode	4,260[c] $20 \times 10 \times 8$	12,852 $40 \times 20 \times 8$	24,738 $40 \times 30 \times 8$	45,264 $40 \times 60 \times 8$
1	51.7	52.3	52.2	52.5
2	102.5	102.6	102.6	102.9
3	151.8	152.7	153.1	153.5
4	192.4	189.9	190.2	190.6
5	254.5	248.5	248.1	248.4
6	282.0	270.5	269.5	269.2
7	381.1	358.6	355.6	354.3
8	414.4	392.7	390.6	389.4
9	524.4	452.3	440.3	430.9
10	536.6	494.4	485.7	476.2
11	613.4	560.0	550.4	540.4
12	700.6	618.6	599.8	573.0
13	777.7	648.7	623.0	604.3
14	802.1	723.7	695.0	665.9
15	851.3	746.1	727.1	704.1
16	887.2	767.9	759.0	743.1
17	989.4	855.9	816.2	779.7
18	1064.4	866.6	846.4	821.6
19	1102.4	955.3	919.2	872.1
20	1160.0	971.8	930.9	900.8

[a]ANSYS FEM, $l \times m \times n$, l = SOLID8 in blade height, m = SOLID8 along chord, n = SOLID8 in thickness.
[b]Design wheel speed $\Omega = V_T/a_T = 261.79$, (rad/s) = 2500, rpm = 41.67 Hz; and frequency ratio $\Omega/\omega_o = 1.5$, where ω_o is the fundamental (lowest) frequency of the stationary fan.
[c]Total degrees of freedom used in the ANSYS FEM analysis.

Table 5 Mode shapes of 3D ROME[a] and ANSYS[b] analyses of rotating baseline composite bypass fan ([0 deg, +45 deg, 0 deg, −45 deg]$_s$ ply-orientation of 0.098 in. (0.249 cm), 0.098 in. (0.249 cm), 0.196 in. (0.498 cm) and 0.49 in. (1.245 cm) ply-thicknesses, respectively)

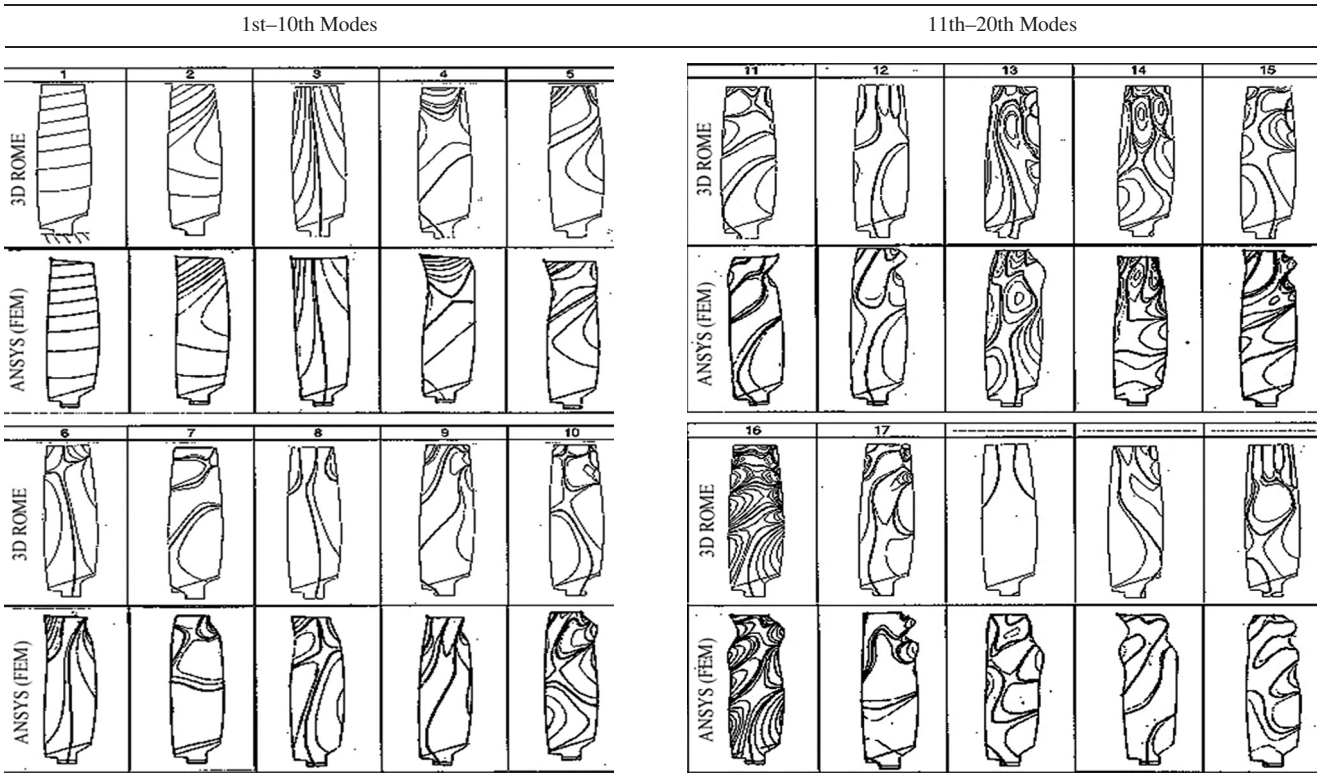

[a]3D ROME 650-term solution, that $\alpha = \beta = \eta = 650$ orthonormal polynomial terms (Eqs. (14)–(17), (22)–(25)) were retained in each of the blade height (u), chord (v), and thickness (w) displacement trial functions, resulting in a solution matrix determinant size of 1950 degrees of freedom.
[b]ANSYS FEM $40 \times 60 \times 8$ grid size, $l \times m \times n$, l = SOLID8 in blade height, m = SOLID8 along chord, n = SOLID8 in thickness.

Depicted in Table 5 are normalized transverse displacement contours for the first 20 modes predicted by the 3D ROME and ANSYS finite element idealizations of the baseline fan (Figs. 1 and 2). Mode shapes are shown for the baseline fan rotating at the design wheel speed ($\Omega = 2500$ rpm). For unidirectional ($\theta_i = 0$ deg) and cross-ply ($\theta_i = 90$ deg) baseline fan blade laminations, deflections in the first five modes can be described as in-phase and out-of-phase rigid body transverse bending displacements and torsional rotations (e.g., first and second flex (1F,2F), and first and second torsion (1T,2T)). Superposition of such rigid body modes does not characterize the chordwise bending mode (1C) since the mode shape describes nodal patterns normal to the blade chord. Increased twist-flex coupling response in all 20 modes can be expected for all angle-ply orientations θ_i, except for unidirectional ($\theta_i = 0$ deg) and cross-ply ($\theta_i = 90$ deg) laminations [13–15,41,49–51].

As can be seen in Table 5, there is strong agreement in the twist-flex coupled response in the first 15 modes that is predicted by each of the 3D ROME and ANSYS finite element calculations. However, a closer examination of the nodal patterns reveals that the 3D ROME and ANSYS calculations predicted different arrangement of modes, and in some instances, the 3D ROME calculations predicted some additional modes. In Table 5 we have attempted to obtain the best match of nodal patterns between the independent mechanical analyses. Shown therein is the mode numbers predicted by the ROME and ANSYS analyses.

6 Aeromechanical Design of a Tailored Vibration and Flutter Controlled High-Bypass Engine Fan

In off-design operation, the frequency margins of the lower flex-torsion modes of a fan may be dangerously close to integral-order resonant and empirical stall flutter boundaries. Primary findings show in Sec. 8 that an optimized mechanical stiffness through material properties (via symmetric angle-ply orientations) and an optimized or mass-balanced fan (via shape variation in blade thickness) can be found to reduce the likelihood of resonant response and flutter on a Campbell diagram. A baseline fan was numerically optimized using a first-of-its-kind reduced-order spectral-based design synthesis extracting explicitly solutions of the simultaneous nonlinear partial differential equations involving the independent design variables (i.e., angle-ply orientations and thickness tuning parameter), which determine the necessary and sufficient Kuhn–Tucker conditions of optimality of constrained minimization. This is formulated in Sec. 7. Solution accuracy and validity of the reduced-order spectral-based design synthesis technology is benchmarked in Sec. 8 against a widely used conventional method of nonlinear programming (i.e., NASA's general-purpose sequential unconstrained minimization technique, Newsumt-A [3]). At this point we described in the following the aeromechanical design considerations used for tailored vibration and flutter suppression of a certain class of composite high-bypass engine fan.

6.1 Frequency Margins on Integral Order Resonance. As stated previously in Sec. 1, a suitable mechanical design assessment of a shroudless composite fan was made entirely on the basis of the possible synchronization of the lower twist-flex frequencies and critical speeds during normal engine operation. The Campbell diagram [4] was the primary design tool. Classical flutter may be suppressed when the flexural center coincides with the center of twist-flex independence and the composite fan is mass balanced about this common center. Given that some tolerance on the radial height mass balancing and flexural center positioning of the baseline composite fan may exist, flutter can be suppressed when the ideal conditions are not exactly satisfied. Here the critical reduced frequency may be away from empirical constraints, and this can optimally be ensured by designing the torsional elastic stiffness of the composite fan sufficiently large, pushing the first torsional frequency sufficiently high as possible on a Campbell diagram [4]. One consideration was to elastically tune the stiffness of composite blades using an optimum pattern of angle-ply lay ups (θ_i) and to mass balance the composite fan using an optimum shape (thickness) distribution (m_T) from dovetail to midradial height of the fan annulus, such that (i) the first flex frequency margin was approximately 15% above 1 per rev [$w_{1f} = 1.15\text{E} = 1.15\Omega$] (with a 2 per rev crossing tolerated near the idle region at approximately 50%–60% of the design wheel speed); (ii) the first torsion mode was pushed as high as possible (above 4 per rev) [$w_{1t} \geq 4\text{E} = 4\Omega$]; and (iii) the second flex mode crossed 3 per rev no higher than 75% of the design wheel speed [$w_{2f,\ 75\%\Omega} \leq 3\text{E} = 3\Omega$].

For maximum efficiency in fluid-dynamic energy transfer by engine fans they are invariably transonic at the tip, and thus, the assumed blade speed must be in the vicinity of the speed of sound in air. As it was presumed akin to industry practice that a constant axial velocity was maintained over the baseline composite fan height, the maximum tip relative velocity was assumed supersonic, i.e., the assumed tip relative Mach number was $V_\infty/a_\infty = 1.3$, where $a_\infty \cong 1117$ (ft/s) (340.7 (m/s)) is the local acoustic velocity. (Relative Mach numbers at the rotor tip up to say 1.5 and corrected tip speeds inside the approximate range of 1150 (ft/s) (350.75 (m/s)) $\leq V_T \leq$ 1480 (ft/s) (451.4 (m/s)) with tip blade angles being less than 65 deg are typical of transonic fans used in advanced bypass engines [43,55–57].) The inlet and exit Mach numbers of the baseline fan was simulated as 0.55 and 0.35, respectively, meeting a empirically based tradeoff between minimal fan frontal area and bypass duct pressure loss.

For less critical stresses at the blade-dovetail interface (Figs. 1 and 2), ensuring sustained mechanical duty, the assumed design wheel speed Ω of the baseline fan (in the dovetail-to-casing ratio (a_H/a_T) range of 0.3, see Table 1) was set to yield a blade tip speed V_T of approximately 1341 (ft/s) (409 (m/s)). Thus, $\Omega = (V_T/a_T) = 261.79$ (rad/s) $= 2500$ rpm, where a_T denotes the fan tip (casing) radius in feet (meters). For moderate-to-large turbofans, speeds in the range of 2500–3600 rpm are typical. The maximum pressure ratio achievable from the baseline fan at the peak of climb was simulated approximately 1.9, where the fan was assumed to operate at its maximum corrected speed in the operating range. As suggested by Walsh and Fletcher [57], the baseline fan was assumed to cruise at a maximum pressure ratio in the range 1.7–1.8, which is suitable for a medium-to-high-bypass ratio fan operating at 0.8 subsonic Mach number. The DeHaller number of the baseline fan was assumed above 0.72, which expressed a baseline technology fan having maximum diffusion factor slightly exceeding those of axial compressors at 0.6 at pitch line and 0.4 at the tip regions [57].

6.2 Empirical Stall Flutter Boundaries. When the flow incidence angle is small, the fan is stable, and when the incidence is near either positive or negative stall, self-excited oscillations of the fan may be induced. The exact mechanism of stall flutter is not fully understood. However, it is known to be associated with periodic flow separation and subsequent reattachment of the flow about the fan blade. Stall flutter cannot be prevented by mass-balancing measures, which tend to uncouple twist-flex motion. Stall flutter suppression is secured by arranging the reduced frequencies at any possible stalling condition constrained at or near empirically acceptable values.

It was the stability of the fan that was most critical to aeroengine operability (i.e., pressure rise capability and efficiency), which was limited by various possible flutter boundaries. As described by Kerrebrock [58], typical flutter boundaries are identified approximately by the regions of the compressor corrected pressure map in which they tend to occur. Supersonic unstalled flutter occurs as corrected speed is increased along the normal operating line. It usually establishes an upper limit to operating speed. Stall flutter may occur as the pressure ratio is increased at fixed corrected speed. For the baseline composite fan, coupled flex-torsion flutter was judged a likely instability concern. Because flex-torsion flutter occurs in a region of the map, where the fan is also susceptible to rotating stall, sometimes flex-torsion flutter may be confused with rotating stall instabilities during fan testing. Choke flutter occurs when the fan is operating with low back-pressure and high flow speeds over the blades.

The instability causing flutter severely degrades blade life through accelerated high-cycle fatigue. Therefore, a high margin between the normal operation of the engine and the various flutter regimes must be maintained during design. An experienced-based approach to ensure that flutter instabilities do not occur in the normal operating range is termed *flutter clearance*. It is difficult to maintain such clearance, because the flutter phenomenon introduces a number of relevant operating parameters not represented on a conventional map of pressure, corrected speed, and weight flow. An accurate experimental clearance of compressor flutter would require an exploration of a four-dimensional map (including temperature or even Reynolds number as well as pressure, corrected speed, and weight flow). This is not pragmatic.

Flutter clearance still is an unpredictable and misunderstood art, which may be only partially achieved by using entirely empirical frequency constraints and recent thermodynamically based metrics [59]. As articulated by Cumpsty [56], "to this day there is no reliable method of predicting the operating boundaries of (fan blade) flutter, and testing the engine over the entire operating range of altitude and speed is the only reliable method of ensuring safe operation." This paper makes a modest alternative step in proposing a reduced-order integrated design synthesis technology that addresses this challenge. Armstrong and Stevenson [60] first observed a mechanism of flow separation from blades during flutter in the lowest order twist-flex modes. Empirical studies have revealed at Reynolds numbers exceeding 2×10^6 stall flutter instabilities do not occur, when sufficient composite fan stiffness is prescribed for twist-flex reduced frequencies not to exceed values empirically well-established for fan flutter suppression in practice. One of Armstrong and Stevenson [60] suggested fan vibration suppression strategies, which is adopted nowadays, is to alleviate the flutter by restaggering the blade tips. Further vibration measurements by Armstrong and Stevenson [60] disclosed empirical values of blade reduced frequency $k = (b\omega/2V_\infty)$—a nondimensional quantity proportional to the product of the twist-flex natural frequency (ω) and the blade semichord ($b/2$), divided by V_∞, the free stream relative velocity—above which stall flutter is an unlikely mechanism of instability for subsonic inlet mass flow near the surge line. The reduced frequency compares the vibrational period of the relevant blade mode to the flow time. Armstrong and Stevenson [60] stipulate for the first flex mode $k_{1f} = (b\omega_{1f}/2V_\infty) = 0.3$ and for the first torsion mode $k_{1t} = (b\omega_{1t}/2V_\infty) = 1.6$ [55]. Wider ranges of empirical values of reduced frequencies (k) for various types of flutter instability and forced response of modern fans were suggested by Kielb [61], e.g., in flutter: $k = 0.1$–0.3 (supersonic and choke bending); $k = 0.4$–0.7 (supersonic unstalled torsion); $k = 0.2$–0.8 (subsonic and transonic stall torsion); and in forced response: $k = 0.1$–1.0 (first flex); $k = 0.4$–2.0 (first torsion); $k = 0.5$–3.0 (second flex); $k = 0.8$–5.0 (second torsion); $k = 1.0$–10.0 (chordwise bending). More liberal ranges of empirical k values for monolithic blades are suggested by Fleeter and Jay [62] and Jay and Fleeter [63]. As far as the present baseline fan design synthesis was concerned, relatively strict reduced frequency constraints were imposed, i.e., $k_{1f} = (b\omega_{1f}/2V_\infty) \geq 0.18$ and $k_{1t} = (b\omega_{1t}/2V_\infty) \geq 0.7$.

6.3 Twist-Flex Coupling Restrictions. Compounding this, it is necessary to consider twist-flex couplings which are due to the aerodynamic forces as the composite fan moves through the air flow, and so attention is confirmed here to the condition where an angle of flow incidence along the fan radial height is small. Flexural loads are induced when the composite fan twists since the radial distribution of the small angles of incidence are altered by the twist motion. Thus, flexural moments are produced by twist deformations. In contrast, flexural deformations of the fan do not alter the radial distribution of the small angles of incidence (provided that the blades are not swept back or forward, or provided that the front-to-back airflow path at the dovetail (which was geometrically dictated by the dovetail slope angle, $\beta_H = 0$ deg, see Fig. 2), so that there is no twisting moment due to the flexural motion, which is structural coupling ascribed to equally symmetrical elasticity or inertia. Aerodynamic couplings are attributed to unsymmetrical flexure, and largely on account of this, the aerodynamic forcing potentially renders the fan unstable. There is thus flexural velocity coupling in the twisting moments. The reason for this is that when the composite fan has a flexural velocity (say downward) the angle of incidence of the air flow relative to the fan is altered (increased). Hence, the blade flexure loading will be increased and there will be an induced twisting moment unless the center of pressure of the additional flexural loading happens to coincide with the flexural center or classically termed a center of twist-flex independence—a kind of averaged aerodynamic center for the composite fan. Hence there is a flexural velocity coupling in the torsional moment, provided the composite fan is constructed with the flexural center at the reference section coinciding with the center of twist-flex independence. On the other side, there is torsional velocity coupling in the flexural moments, provided there are oftentimes negligible higher-order effects of aerodynamic twist-flex coupling accelerations arising from radial distribution of fan product moment of inertia.

Consequently, it was also desirable to minimize the amount of twist in the first flex mode. This twist-flex coupling was influenced not only by the angle-ply orientations, but also by the front-to-back airflow path at the dovetail (which was geometrically dictated by the dovetail slope angle, $\beta_H = 12.5$ deg, see Fig. 2). Here an additional constraint was imposed which limits the twist-flex coupling in the first flex mode $\zeta_{1t-f} = b\alpha/(2\Delta_b)$, to less than say 0.2, where Δ_b was the relative transverse bending displacement causing an aerodynamically destabilizing wash-in effect, and α was the relative twist displacement measured along a cross-sectional meridian line connecting the blade's leading and trailing edges. In the present fan design synthesis, the twist-flex coupling parameter ζ was measured at midchord of a section taken beyond the mean radius of the fan (say at the tip of the blade height).

6.4 First-Ply-Failure Steady-Stress Limitations. For metal alloy fans, the tip speeds and axial velocity are constrained to yield a suitable level of relative gas velocity since compressibility effects are more critical than mechanical stress considerations. For laminated composite fans, however, the mass ratio is substantially lower and a design check on mechanical stress levels, albeit not critical, is justifiable to ensure that the composite tailoring is protected against fibrous composite delamination and damage. An acceptable laminate design must withstand two primary sources of steady stress, which are peak at the dovetail (Figs. 1 and 2). These are (i) the centrifugal tensile stress, and (ii) the bending stress due to steady-state, axial, and tangential gas flow-induced loads averaged over finite strips of the blade height. The principal (first-ply failure) orientation of these steady stresses must be below the material stress limits of the composite blade fibers.

In an actual engine fan, the centrifugal tensile stress is steady, whereas the gas flow-induced bending stress is quasi-steady as the fan blades pass through nonuniform flow distributions. According to Cohen et al. [43], the gas flow-induced bending stress is directly proportional to the blade height and fan stage work output (i.e., a product of the inlet mass flow and whirl velocity), and inversely proportional to the number of blades and the hub section modulus. (The latter is a function of the blade camber and thickness-to-chord ratio). Moreover, the centrifugal bending stress, which is highly sensitive to blade manufacturing imperfections and blade root fixing, may cancel the gas flow-induced bending stress at the design wheel speed, when the schedule of blade radial sections is inclined relative to any radial line. In the present fan design synthesis calculations, the schedule of blade centroids was assumed nearly radial. Hence, the centrifugal bending stress was negligible.

6.5 Appropriate Sets of Side Constraints. One set of side constraints required that the permissible angle between adjacent ply layers be limited to 45 deg. An additional set of side constraints limited the angle-ply orientation of ply layers to be within the range of ± 90 deg. For a physically reasonable tailored design

for vibration suppression of the baseline fan, the limit of thickness tuning variable m_T was set between −20 deg and −70 deg.

7 Fan Design as a Constrained Minimization

In this section a formal definition of the constrained fan design using stiffness tailoring and shape optimization is summarized, and a method for finding the optimum fan stiffness (via angle-ply lay-ups) and fan thickness from dovetail-to-midblade height is discussed. The steps taken are: first, to define the objective function, which was to maximize the frequency of the first torsion mode of the fan; second, to define the set of constraints which were satisfied; and third, to solve this constrained minimization problem using a reduced-order spectral-based design synthesis (optimization) technique newly developed for this work.

7.1 Mathematical Nonlinear Optimization Problem Statement of the Baseline Fan Redesign. First, a mathematical statement of the objective cost function is as follows: Find an optimum fan thickness (i.e., a shape parameter m_T) along with optimum fan stiffness (i.e., a set of noninteger-valued angle-ply orientations, θ_i) in which the first torsion mode was maximized (i.e., the first torsion mode was pushed as high as possible):

$$\max F(\theta_i, m_T) = \max(\omega_{1t}) \tag{41}$$

which is equivalent to

$$\min H(\theta_i, m_T) = \min(-\omega_{1t}) \tag{42}$$

Next, we mathematically state the following set of constraints.

Frequency margins on integral order resonance:

$$g_1(\theta_i, m_T) = \frac{\omega_{1f}}{1.15\Omega} - 1 \geq 0 \tag{43}$$

$$g_2(\theta_i, m_T) = \frac{\omega_{1t}}{4\Omega} - 1 \geq 0 \tag{44}$$

Empirical stall flutter boundaries:

$$g_3(\theta_i, m_T) = \frac{k_{1f}}{0.18} - 1 \geq 0 \tag{45}$$

$$g_4(\theta_i, m_T) = \frac{k_{1t}}{0.7} - 1 \geq 0 \tag{46}$$

Twist-flex coupling restriction at the fan tip:

$$g_5(\theta_i, m_T) = 1 - \frac{\zeta_{1t-f}}{0.2} \geq 0 \tag{47}$$

($\zeta_{1t-f} = b\alpha/(2\Delta_b)$ being twist-flex coupling in the first flex mode with Δ_b defining the relative transverse bending displacement causing an aerodynamically destabilizing wash-in effect, α representing the relative twist displacement measured along a cross-sectional meridian line connecting the blade's leading and trailing edges, and ζ measured at midchord of a section taken beyond the mean radius of the fan (say at the tip of the blade height).)

Second flex mode below 3 *per rev* crossing at 75% speed:

$$g_6(\theta_i, m_T) = 1 - \frac{\omega_{2f,75\%\Omega}}{3\Omega} \geq 0 \tag{48}$$

First-ply-failure steady stress:

$$g_7(\theta_i, m_T) = 1 - \left[\left(\frac{\sigma_x}{\sigma_{Lu}}\right)^2 - \left(\frac{\sigma_x}{\sigma_{Lu}}\right)\left(\frac{\sigma_y}{\sigma_{Tu}}\right) + \left(\frac{\sigma_y}{\sigma_{Tu}}\right)^2 + \left(\frac{\sigma_{xy}}{\sigma_{LTu}}\right)^2\right] \geq 0 \tag{49}$$

Permissible angle between adjacent ply layers:

$$g_{7+k}(\theta_i, m_T) = 1 - \frac{(\theta_k - \theta_{k+1})}{45 \text{ deg}} \geq 0 \tag{50}$$

Side constraints on the fan stiffness (angle-ply orientations):

$$-\frac{\pi}{2} \leq \theta_i \leq \frac{\pi}{2} \tag{51}$$

Side constraints on the shape (thickness) parameter:

$$-70 \text{ deg} \leq m_T \leq -20 \text{ deg} \tag{52}$$

In Eqs. (41)–(52), $i = 1,2,\ldots,(N_p/2)$, and $k = 1,2,\ldots,(N_p/2) - 1$, where N_p denotes the total number of plies of the blade laminate, and the total number of inequality constraints are $j = 1,2,\ldots,N_g$, where $N_g = 7 + k$. The constraint Eq. (60) is the classical first-ply-failure criterion for laminated composite structures proposed by Azzi and Tsai [64], where σ_{L_U}, σ_{T_U}, and σ_{LT_U} are ultimate strength values of longitudinal (L), transverse (T), and shear (LT) principal ply stresses.

The mathematical optimization statement of the baseline composite fan redesign has now been completely defined. The baseline composite fan (Figs. 1 and 2, and Table 1) was numerically optimized using a first-of-its-kind reduced-order spectral-based design synthesis predicting solutions of the simultaneous nonlinear partial differential equations involving the independent design variables (i.e., angle-ply orientations θ_i, thickness tuning parameter m_T, and slack variables or Lagrange multipliers λ_j), which determine the necessary and sufficient Kuhn–Tucker conditions of optimality of constrained minimization [25,37,65–71], which are defined in the next section. Solution accuracy and validity of the present reduced-order design synthesis technology is benchmarked against a widely used conventional method of nonlinear programming (via. sequential unconstrained minimization technique). The baseline fan Campbell diagram was optimally restructured with wider resonant frequency margins at low integral orders that (1) achieved multiple frequency margins while maintaining proper clearance from multiple empirical stall flutter boundaries, (2) controlled twist-flex coupling at the blade tips in the lowest (fundamental) mode, and (3) ensured the mechanical strength integrity through maximum restrictions placed on steady centrifugal tension and to a lesser extent gas flow-induced bending stresses (assumed negligible in the present fan design).

An additional set of side constraints was imposed to ensure that the angle-ply stacking sequence was of acceptable form for manufacturing. The last step is to numerically calculate the suitable pattern of angle-ply orientations, which results in a constrained maximum. It was proper to introduce a Lagrangian function as a sum of the objective function, plus the constraint functions multiplied by Lagrange multipliers. The necessary conditions for a global optimum of the objective cost function and associated constraints was determined by the Kuhn–Tucker conditions of optimality explicitly imposed in the newly developed reduced-order analysis of nonlinear mathematical programming (briefly outlined in Sec. 7.3).

7.2 Definition of the Necessary and Sufficient Kuhn–Tucker Optimality Conditions Employed. As the constrained fan design problem was a convex programming problem for extrema (in other words, the objective cost function (Eq. (41)) was convex (or Eq. (42) was concave) and the design constraint functions (Eqs. (43)–(52)) were concave), then the fan design problem could satisfy the following conditions and also could be determined as convex. For any pair of design points, (θ_i^1, m_T^1) and (θ_i^2, m_T^2),

$$H[\alpha(\theta_i^2, m_T^2) + (1-\alpha)(\theta_i^1, m_T^1)] \leq \alpha H(\theta_i^2, m_T^2) + (1-\alpha)H(\theta_i^1, m_T^1) \tag{53}$$

$$g_j[\alpha(\theta_i^2, m_T^2) + (1-\alpha)(\theta_i^1, m_T^1)] \le \alpha g_j(\theta_i^2, m_T^2) + (1-\alpha) g_j(\theta_i^1, m_T^1) \tag{54}$$

such that $0 < \alpha < 1$ [69]. As Eqs. (53) and (54) were satisfied, the fan design (Eqs. (41)–(52)) had two distinct properties [70]. First, any local optimum of Eqs. (41)–(52) was a global optimum at the design point (θ_i^*, m_T^*). Second, the necessary and sufficient conditions for a global optimum (θ_i^*, m_T^*) was that there exist a set of dual variables or Lagrange multipliers λ_j^*, that satisfied the Kuhn–Tucker optimality conditions [25,37,65–71]:

$$g_j(\theta_i^*, m_T^*) \ge 0 \tag{55}$$

$$\lambda_j^* \ge 0 \tag{56}$$

$$\frac{\partial H}{\partial \theta_i}(\theta_i^*, m_T^*) + \frac{\partial H}{\partial m}(\theta_i^*, m_T^*) + \sum_{j=1}^{Ng} \lambda_T^* \frac{\partial g_j}{\partial \theta_i}(\theta_i^*, m_T^*) + \frac{\partial g_j}{\partial m}(\theta_i^*, m_T^*) = 0 \tag{57}$$

$H(\theta_i, m_T)$ (Eq. (42)) and $g_j(\theta_i, m_T)$ (Eqs. (43)–(52)) was once continuously differentiable. Hence, Eqs. (55)–(57) were first-order sufficiency conditions of global optimality. They were stationary conditions of the Lagrangian function,

$$\varphi(\theta_i, \lambda_j) = H(\theta_i, m_T) + \sum_{j=1}^{Ng} \lambda_j g_j(\theta_i, m_T) \tag{58}$$

with respect to the primal (θ_i, m_T) and dual λ_j variables (Lagrange multipliers). These Lagrange multipliers were defined as a ratio of sensitivities of the objective (cost) function with respect to the primal variables to the sensitivity of the constraint functions with respect to the primal variables. The Kuhn–Tucker conditions [25,37,65–71] (Eqs. (55)–(57)) were a powerful test of optimality for the fan design solution of Eqs. (41)–(52). Geometrically speaking, the Kuhn–Tucker conditions defined an ideal cone (or multidimensional pyramid) expressed by the normal to the active constraints at the optimum design, defined as $\partial g_j(\theta_i^*, m_T^*)/\partial\theta_i$ [69]. Then, the Kuhn–Tucker conditions examined whether the gradient of the objective cost function at the optimum design, defined as $\partial H(\theta_i^*, m_T^*)/\partial\theta_i$, was contained inside the pyramid. As this was the case, the Kuhn–Tucker optimality conditions were satisfied.

Practical application of the Kuhn–Tucker optimality test [69] requires, in contrast, a solution of the simultaneous linear equations in λ_j

$$\sum_{j=1}^{N_g} \frac{\eta_{ij}}{\chi_j} \lambda_j = [e_{ij}]\{\lambda_j\} = \{1\} \tag{59}$$

where $\eta_{ij} = \partial g_i/\partial\theta_j$, $\chi_j = \partial F/\partial\theta_j$, and $[e_{ij}]$ is a matrix of Lagrangian energy densities, which represents a ratio of gradients of the constraint functions and the objective function. Equations (59) are a rewrite of the conditions of optimality (Eqs. (57)). If one considers the residual

$$\Lambda_{Ri} \equiv \sum_{j=1}^{N_g} \eta_{ij}\lambda_j - \chi_j \tag{60}$$

having the norm $|\Lambda_{Ri}|^2 \equiv \lfloor \Lambda_{Ri} \rfloor \{\Lambda_{Ri}\}$, then the stationary conditions of the residual norm as a function of λ are

$$\frac{\partial \Lambda_{Ri}}{\partial \lambda_i} \equiv \left([\eta_{ij}]^T [\eta_{ij}] \right) \{\lambda_{ij}\} - [\eta_{ij}]^T \{\chi_j\} = 0 \tag{61}$$

from which

$$\{\lambda_{ij}\} \equiv \left([\eta_{ij}]^T [\eta_{ij}] \right)^{-1} [\eta_{ij}]^T \{\chi_j\} \tag{62}$$

Thus if all $\{\lambda_j\} > 0$ from Eq. (63), and if λ_j satisfy Eq. (57), then the Kuhn–Tucker optimality test was satisfied. This important optimality test will be examined further in the discussion of results.

7.3 Reduced-Order Spectral-Based (ROS) High-Bypass Fan Design Synthesis. A first-of-its-kind reduced-order spectral-based (ROS) design synthesis is described in this section for explicitly and directly determining the solutions of the simultaneous nonlinear partial differential equations (Eqs. (55)–(57)) (in terms of the design variables (θ_i, m_T) and slack variables or Lagrange multipliers λ_j), characterizing the necessary and sufficient Kuhn–Tucker first-order stationary conditions of optimality of constrained minimization [25,37,65–71]. Solution accuracy and validity of the present ROS design synthesis technology was benchmarked against a widely used conventional method of nonlinear programming (via sequential unconstrained minimization technique), which is described in the next section.

Consider now the set of present fan design variables (θ_i, m_T) represented mathematically here as an Euclidean n-dimensional design vector space $\{X\} = \{x_1, x_2 \ldots, x_n\}^T$. Let the objective (cost) function $H(\theta_i, m_T)$ (Eq. (42)) and constraints $g_j(\theta_i, m_T)$ (Eqs. (43)–(52)), collectively for now be represented as $f(X) = f(x_1, x_2, \ldots, x_n)$ of several variables in the assumed Euclidean n-dimensional design vector space $\{X\}$, which can be approximated by using a generalized Fourier series of orthonormal polynomials in several variables, which are mathematically complete [38–40], evaluated at a selected set of $\{X^a\}$,

$$[\Phi(x_1^a, x_2^a, \ldots, x_n^a)]\{q\} = \{f(x_1^a, x_2^a, \ldots, x_n^a)\} \tag{63}$$

The unknown generalized coefficients $\{q\}$ was calculated as

$$[\Phi(X^a)]^T [\Phi(X^a)]\{q\} = [\Phi(X^a)]^T \{f(X^a)\} \tag{64}$$

$$\{q\} = [\Phi(X^a)]^T \{f(X^a)\} \tag{65}$$

The gradient $\partial f / \partial x_j$ at $\{X^a\}$ is calculated by taking the derivative of the assumed orthonormal polynomials $\Phi(X)$, as follows:

$$\frac{\partial f}{\partial x_j} = f_{,j}(X^a) = [\Phi_{,j}(X^a)]^T \{q\} \tag{66}$$

An assumed recursive formulae for Φ_k in Euclidean n-dimensional design space x_n is

$$\Phi_k(x_1, x_2, \ldots, x_n) = \frac{{}^{(i)}a_k(x_1, x_2, \ldots, x_n)}{\text{Norm}[{}^{(i)}a_k(x_1, x_2, \ldots, x_n)]} \tag{67}$$

where ${}^{(i)}a_k(x_1, x_2, \ldots, x_n)$ is the kth generating polynomial term of the ith calculating step. For the first iteration, $i = 1$, the definition of the kth generating polynomial term is

$${}^{(1)}a_k(x_1, x_2, \ldots, x_n) = \left[\sum_{l=0}^{N} \sum_{m=0}^{l} \cdots \sum_{q=0}^{p} (x_1^{l-m} x_2^{m-n} \cdots x_n^q) \right] \tag{68}$$

where l, m, p, q are integers for the polynomial terms leading to a total number of series terms N. The first term $(k = 1)$ of the orthonormal polynomials (Φ_k) is

$$\Phi_1(x_1, x_2, \ldots, x_n) = \frac{{}^{(1)}a_1(x_1, x_2, \ldots, x_n)}{\text{Norm}[{}^{(1)}a_1(x_1, x_2, \ldots, x_n)]} \tag{69}$$

For calculating steps $i = 2,3,\ldots,N$, each generating polynomial is updated using the following:

$$r_{k-1,k} = \int_v \Phi_{k-1}(x_1,x_2,\ldots,x_n)({}^{(i-1)}a_k(x_1,x_2,\ldots,x_n))dv$$
$${}^{(i)}a_k(x_1,x_2,\ldots,x_n) = {}^{(i-1)}a_k(x_1,x_2,\ldots,x_n) - \Phi_{k-1}(x_1,x_2,\ldots,x_n)r_{k-1,k} \tag{70}$$

for $k=i,\ldots,N$. Equations (70) orthogonalize all of the generating polynomials of the ith calculating step (${}^{(k)}a_k$) to the $(k-1)$th orthonormalized polynomials (Φ_{k-1}). The kth orthonormal polynomial term (Φ_k) is obtained by normalizing the${}^{(k)}a_k$ by Eqs. (15). For any obtained orthonormal polynomials Φ_k, then $\Phi_k^T\Phi_k = 1$, and $\Phi_i^T\Phi_j = 0 (i \neq j)$.

The first gradient $\Phi_{k,j}(x_1,x_2,\ldots,x_n)$ with respect to x_j $(j=1,2,\ldots,n)$ is defined as

$$\Phi_{k,j}(x_1,x_2,\ldots,x_n) = \frac{{}^{(i)}a_{k,j}(x_1,x_2,\ldots,x_n)}{\text{Norm}[{}^{(k)}a_k(x_1,x_2,\ldots,x_n)]} \tag{71}$$

where ${}^{(i)}a_{k,j}(x_1,x_2,\ldots,x_n)$ is the gradient of kth generating polynomial with respect to $x_j (j=1,2,\ldots,n)$. ${}^{(i)}a_k$ is obtained from Eqs. (70). For the first iteration $i=1$,

$${}^{(1)}a_{k,j}(x_1,x_2,\ldots,x_n) = \left[\sum_{l=0}^{N}\sum_{m=0}^{l}\cdots\sum_{q=0}^{p}(x_1^{l-m}x_2^{m-n}\cdots x_n^q)\right]_{,j} \tag{72}$$

For any $i=2,3,\ldots,N$, the first derivative of every generating polynomial is written as

$${}^{(i)}a_{k,j}(x_1,x_2,\ldots,x_n) = {}^{(i-1)}a_{k,j}(x_1,x_2,\ldots,x_n) - \Phi_{(k-1),j} \times (x_1,x_2,\ldots,x_n)r_{k-1,k} \tag{73}$$

for $k=i,\ldots,N$. where $r_{k-1,k}$ is obtained from Eq. (70). The first derivative of the assumed kth polynomial term ($\Phi_{k,j}$) is obtained by normalizing the${}^{(k)}a_{k,j}$ by Eq. (71).

Substituting Eqs. (63)–(73) into Eqs. (55)–(57) establish the ROS design synthesis technology. A computational algorithm was developed in this work that constructs (i) the simultaneous nonlinear partial differential equations (55)–(57) (in terms of the design variables (θ_i, m_T) and slack variables or Lagrange multipliers λ_j), (ii) the multivariate orthonormal polynomial approximation equations (63)–(73), and (iii) upon substituting (ii) into (i) the resulting nonlinear algebraic equations in the unknown generalized coefficients $\{q\}$, which were efficiently solved using a quasi-Newton procedure presented elsewhere [52].

7.4 Nonlinear Constrained Minimization via Augmented Lagrangian and Sequential Unconstrained Minimization Technique (SUMT). The present fan design is a nonlinear mathematical programming (NMP) problem (defined in Sec. 7.1) in which noninteger-valued angle-ply orientation angles θ_i and the blade thickness parameter m_T are the primary design variables. In a general sense, the NMP problem may be stated as: Find θ_i and m_T, which minimizes an objective function, $H(\theta_i, m_T)$ (Eq. (42)), subjected to primary constraints, $g_j(\theta_i, m_T) \geq 0$ (Eqs. (43)–(50)), and side constraints, $-\pi/2 = \theta^{(L)} \leq \theta_i \leq \theta^{(U)} = \pi/2$ (Eq. (51)) and -70 deg $\leq m_T \leq -20$ deg (Eq. (52)).

As validation of the correctness and accuracy of optimum fan design solutions predicted using the developed ROS design synthesis technology described in Secs. 7.2 and 7.3, the NMP problem (Sec. 7.1) was also solved using Newsumt-A [3], which is an open-source FORTRAN computer program for the solution of nonlinear inequality constrained or unconstrained function minimization problems. The basic algorithm is a sequential unconstrained minimization technique (SUMT) [3,71] using a modified Newton's method for calculating the search directions of the unconstrained minimization. Basically, in using Newsumt-A [3], the NMP problem is solved as a sequence of unconstrained minimization problems mathematically transformed into an extended penalty function (or augmented Lagrangian):

$$\phi(\theta_i, m_T, r_p) = H(\theta_i, m_T) + r_p\left(\sum_{j=1}^{N_g}\Psi_j + \sum_{i=1}^{N_p}\Upsilon_i\right) \tag{74}$$

where Ψ_j and Υ_i represent functions involving the constraint functions $g_j(\theta_i, m_T) \geq 0$ and the side constraints, $\theta^{(L)} \leq \theta_i \leq \theta^{(U)}$, respectively. In addition, Ψ_j and Υ_i involved a control parameter which maintained overall numerical stability and ensured a feasible solution. In Newsumt-A [3] the composite function $\phi(\theta_i, m_T, r_p)$ defined in Eq. (74) has been modified to improve feasibility at intermediate designs and to accelerate one-dimensional searches. The composite function is minimized for a specified value of the penalty parameter by calculating a search direction and a step length and then updating the design. The search direction in Newsumt-A is generalized from a modified Newton's approach involving a Hessian operation and gradient $\nabla\varphi$ of the composite function $\phi(\theta_i, m_T, r_p)$ defined in Eq. (74). A golden section algorithm used to calculate the associated step length. The r_p was assumed a positive constant known as a penalty multiplier, akin in nature to the $\{\lambda_j\} > 0$ from Eq. (56). The composite function $\phi(\theta_i, m_T, r_p)$ is optimized with diminishing penalty parameter r_p until convergence occurs. A constrained minimum of $H(\theta_i, m_T)$ was obtained by determining the unconstrained minimum of $\phi(\theta_i, m_T, r_p)$ for a decreasing sequence of r_p. For small r_p, finding the minimum of $\phi(\theta_i, m_T, r_p)$ was locally equivalent to finding the stationary points of $H(\theta_i, m_T)$. The SUMT nonlinear programming technique has been successfully used in structural design optimization during the past three decades. Overall, Newsumt-A [3] appears to be a precise and reliable nonlinear programming software for the design optimization of structural systems. Newsumt-A [3] can, however, be expensive, requiring numerous reanalysis computations depending on the design problem considered.

This is the foundation of the Newsumt-A [3] methodology, known as nonlinear programming via augmented Lagrangian, as similarly achieved by substituting Eqs. (63)–(73) into Eqs. (55)–(57) in establishing the present ROS design synthesis technology, whose design solutions of finding θ_i and m_T which minimizes $H(\theta_i, m_T)$ (Eq. (53)), subjected to constraints $g_j(\theta_i, m_T) \geq 0$ (Eqs. (43)–(50)), and side constraints, $-\pi/2 = \theta^{(L)} \leq \theta_i \leq \theta^{(U)} = \pi/2$ (Eq. (51)) and -70 deg $\leq m_T \leq -20$ deg (Eq. (52)), are compared against those design solutions θ_i and m_T predicted by Newsumt-A [3]. In both the Newsumt-A and present ROS design synthesis analyses, the constraints $g_j(\theta_i, m_T) \geq 0$ was normalized such that they vary between 0 and 1. The latter constraint normalization ensured a rapid convergence rate during the minimization of $\phi(\theta_i, m_T, r_p)$. Sensitivity derivatives of $\phi(\theta_i, m_T, r_p)$ were approximated inside Newsumt-A [3] using finite differences with minimal function evaluations. In contrast, sensitivity derivatives using the present ROS design synthesis technology were determined using Eq. (66).

As the convexity conditions, Eqs. (53) and (54), were satisfied, the fan design (Eqs. (41)–(52)), as previously noted, had two distinct properties [70]. First, any local optimum of Eqs. (41)–(52) was a global optimum at the design point (θ_i^*, m_T^*). Second, the necessary and sufficient conditions for a global optimum (θ_i^*, m_T^*) was that there exist a set of dual variables r_p, or Lagrange multipliers λ_j^*, that satisfied the Kuhn–Tucker optimality conditions [25,37,63–71] (see Eqs. (55)–(57)). Hence, the improved SUMT algorithm employed in the Newsumt-A software package [3] was empirically stable and computationally efficient for the present fan designs. In using the Newsumt-A software package [3], the baseline fan design having critically active constraints as well as passive ones was redesigned towards the center of the feasible design region (as ideally depicted in Fig. 8). Subsequent

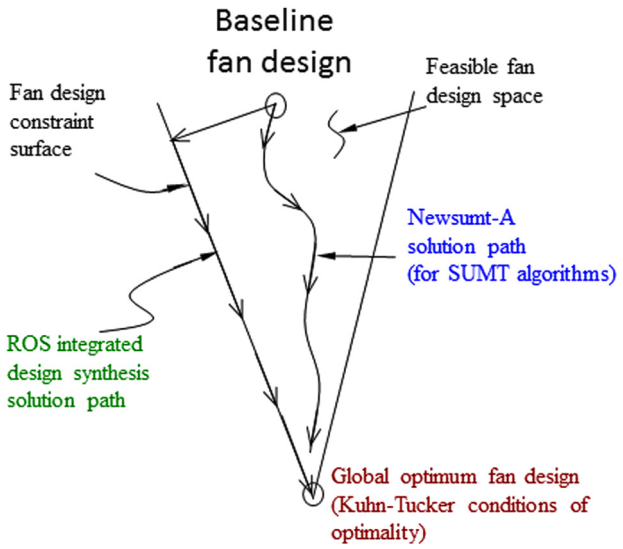

Fig. 8 ROS and Newsumt-A [3] paths of solution convergence from baseline to global optimum fan designs

redesigns funnel down the middle of the feasible region (Fig. 8) yielding a sequence of improved designs with passive and/or noncritical constraints. That is, the unconstrained minima of the compound function, all lie within the feasible design region for all r_p. Ideally, Newsumt-A [3] should generate a final blade design, which satisfies all the design restrictions, and which is at least a local minimum (that is, where $\phi(\theta_i, m_T, r_p)$ converges to $H(\theta_i, m_T)$, see Eq. (74)). Complete details of the fundamental procedures used in the Newsumt-A software are given elsewhere [3]. While the Newsumt-A general-purpose software [3] did not solve Eqs. (55)–(57) explicitly as the present ROS design synthesis technology did, the fan design optimization studies in the next section compares satisfaction of the necessary and sufficient Kuhn–Tucker conditions of global optimality achieved by the Newsumt-A and present ROS fan designs, validating the solvability, consistency, and accuracy of the ROS design synthesis methodology.

8 Discussion of Fan Design Optimization Studies

Summarized in Tables 6 and 7 is the ROS (Eqs. (55)–(57), (63)–(73)) and Newsumt-A [3] optimum design histories of the 16-ply and 32-ply baseline fans operating at the design wheel speed Ω. Ensuring minimal critical stresses at the blade-dovetail interface (Figs. 1 and 2), the assumed $\Omega = (V_T/a_T) = 261.79$ (rad/s) $= 2500$ rpm $= 41.67$ Hz, for a frequency ratio $\Omega/\omega_o = 1.5$, where ω_o was the fundamental (lowest) frequency of the baseline stationary fan). Recall that the assumed Ω was set for the baseline fan (having a dovetail-to-casing ratio, $a_H/a_T = 0.3$, see Table 1) to yield a blade tip speed V_T of approximately 1341 (ft/s) (409 (m/s)), a_T being the fan tip (casing) radius in feet (meters). Listed in Tables 6 and 7 are the results of design constraints and objective (cost) function solutions of the fan design. The baseline 16-ply and 32-ply fans were created by subdividing the layers of the baseline 8-ply fan analyzed using 3D ROME and ANSYS finite element technologies in Sec. 5. Again, the stiffness (angle-ply orientations θ_i $(i = 1,2,\ldots,N_{plies})$) of the baseline fans were nominally assumed as [0 deg, +45 deg, 0 deg_2, –45 $deg_5]_s$ (subscripted numbers denote ply-layers) with 0.098 in. (0.249 cm) ply-thickness for the 16-ply lay-up fan, and as [0 deg_2, +45 deg_2, 0 deg_4, –45 $deg_{10}]_s$ with 0.049 in. (0.1245 cm) ply-thickness for the 32-ply lay-up fan. Symmetric placement of the angle plies θ_i $(i = 1,2,\ldots,N_{plies})$ about the middle plane of the baseline fan blades were assumed, as a sufficient restriction of certain combinations of in-plane and bending stiffness effects [13–15,41,51]. The laminate designs consist of two symmetric sublaminates with equal numbers of plies and equal but arbitrary angle-ply orientations θ_i $(i = 1,2,\ldots,N_{plies}/2)$. In comparison to the baseline frequencies shown in Table 3, one can see in Tables 6 and 7 that a slight increase in the first and second flex and first torsion frequencies was predicted by the 100-term 3D ROME baseline fan free vibration response solutions assumed in the ROS and Newsumt-A [3] optimization analyses, as shown in Tables 6–9. As can be seen in Tables 6 and 7, most of the constraint values for the infeasible baseline blade were passive ($g_j > 0$), except for the active constraints on the first torsion mode ω_{1t} $(g_2 = -0.1)$ (Eq. (44)) and the first torsion reduced frequency k_{1t} $(g_4 = -0.2)$ (Eq. (46)). The maximum permissible fan design stiffness (orientation angle between adjacent angle plies) was set to ± 45 deg (see Eq. (50)). Hence, the stiffness (angle-ply orientations) of the baseline fan design was located on an active constraint boundary in the infeasible region of the overall design space.

The optimum solutions exist when the cost function $C(\theta_i, m_T)$ and the compound total function $\phi(\theta_i, m_T, \lambda_j)$ are equal. It can be seen in Table 6(*a*) the functions $|C| \approx |\phi| \approx 186$ (Hz) and in Table 7(*a*) the functions $|C| \approx |\phi| \approx 186$ (Hz) were judged accurately converged using the present ROS design synthesis technology. By contrast in Table 6(*b*), the Newsumt-A [3] functions $|C| \approx |\phi| \approx 188$ (Hz) and in Table 7(*b*) the Newsumt-A [3] functions $|C| \approx |\phi| \approx 191$ (Hz) are slightly less converged compared to the ROS technology. Yet, the cost and total functions were judged

Table 6 (*a*) ROS and (*b*) Newsumt-A [3] optimum design and constraints for 16-ply composite bypass fan operating at the design wheel speed Ω ([0 deg, +45 deg, 0 deg_2, −45 $deg_5]_s$ ply-orientation (subscripted numbers denote ply-layers) of 0.098 in. (0.249 cm) ply-thickness)

Design surface	Cost $\|C\|$	Total $\|\phi\|$	ω_{1f}	ω_{2f}	ω_{1t}	k_{1f}	k_{1t}	$\zeta_{1t\text{-}f}$	75% Ω ω_{2f}	$\sigma_{failure}$
(a) Baseline g_j	–	–	0.1	–	−0.1	0.1	−0.2	0.31	0.05	0.6
Baseline	147.9	–	52.7	105.1	147.9	0.2	0.57	0.14	88.7	0.4
Optimum	**185.9**	**185.1**	**51.4**	**110.4**	**185.9**	**0.2**	**0.7**	**0.1**	**95.9**	**0.1**
Final g_j	–	–	0.1	–	0.1	0.1	0.0	0.48	−0.02	0.9
Rounded g_j[a]	186.1	–	0.1	–	0.1	0.1	0.1	0.5	0.00	0.9
(b) Baseline g_j	–	–	0.1	–	−0.1	0.1	−0.2	0.31	0.05	0.6
Baseline	147.9	–	52.9	105.4	147.9	0.21	0.58	0.14	89.1	0.4
1	194.4	−170.2	55.7	110.4	194.4	0.22	0.75	0.08	95.0	0.6
2	186.4	120.8	52.9	109.8	186.4	0.21	0.72	0.10	93.4	0.6
3	187.5	179.8	53.1	110.2	187.5	0.21	0.73	0.09	92.9	0.6
4	187.8	186.0	53.4	111.1	187.8	0.21	0.73	0.09	93.5	0.6
Optimum	**188.6**	**188.3**	**53.5**	**111.2**	**188.6**	**0.21**	**0.73**	**0.09**	**93.6**	**0.6**
Final g_j	–	–	0.1	–	0.1	0.2	0.0	0.5	0.00	0.4
Rounded g_j[a]	189.3	–	0.1	–	0.1	0.1	0.0	0.5	0.00	0.4

[a]Fan design as optimized fan stiffness (angle-ply orientations) are rounded to nearest 5 deg.

Table 7 (*a*) ROS and (*b*) Newsumt-A [3] optimum design and constraints for 32-ply composite bypass fan operating at the design wheel speed Ω ([0 deg$_2$, +45 deg$_2$, 0 deg$_4$, −45 deg$_{10}$]$_s$ ply-orientation (subscripted numbers denote ply-layers) of 0.049 in. (0.1245 cm) ply-thickness)

Design surface	Cost $\|C\|$	Total $\|\phi\|$	ω_{1f}	ω_{2f}	ω_{1t}	k_{1f}	k_{1t}	$\zeta_{1t\text{-}f}$	75% Ω ω_{2f}	σ failure
(a) Baseline g_j	–	–	0.1	–	−0.1	0.1	−0.2	0.31	0.05	0.6
Baseline	147.9	–	52.7	105.1	147.9	0.2	0.57	0.14	88.7	0.4
Optimum	**185.7**	**185.5**	**52.4**	**110.5**	**185.5**	**0.2**	**0.7**	**0.1**	**95.3**	**0.1**
Final g_j	–	–	0.1	–	0.1	0.1	0.0	0.48	−0.02	0.9
Rounded g_j[a]	186	–	0.1	–	0.1	0.1	0.1	0.5	0.0	0.9
(b) Baseline g_j	–	–	0.1	–	−0.1	0.1	−0.2	0.31	0.05	0.6
Baseline	147.9	–	52.7	105.1	147.9	0.20	0.57	0.14	88.7	0.4
1	192.5	−114.9	53.9	109.6	192.5	0.21	0.75	0.09	94.1	0.1
2	188.7	147.9	52.2	109.1	188.7	0.20	0.73	0.12	92.6	0.1
3	190.2	184.1	52.9	110.4	190.2	0.21	0.74	0.11	93.2	0.1
4	191.9	190.6	52.6	111.2	191.9	0.20	0.74	0.11	93.5	0.1
5	192.1	191.5	52.4	111.4	192.1	0.20	0.74	0.11	93.7	0.1
Optimum	**191.3**	**191.3**	**52.5**	**111.3**	**191.3**	**0.20**	**0.74**	**0.11**	**93.7**	**0.1**
Final g_j	–	–	0.1	–	0.1	0.1	0.1	0.4	0.0	0.9
Rounded g_j[a]	190.6	–	0.1	–	0.1	0.1	0.1	0.5	0.0	0.9

[a]Fan design as optimized fan stiffness (angle-ply orientations) are rounded to nearest 5 deg.

automatically within Newsumt-A [3] suitably converged after four and five iterative redesign surfaces formed in Newsumt-A [3]. More important in Tables 6 and 7 are the final design constraint values $g_j(\theta_i, m_T) \geq 0$ (Eqs. (43)–(52)), which suggests that all constraints were essentially passive. In the final design, the potentially most active constraint (indicated by the g_j value closest to zero or slightly negative) was the one imposed on the second flex mode at 75% speed lower than 3 per rev, $\omega_{2f,75\%\Omega} < 3E = 3\Omega$ ($g_6 \cong 0$) (Eq. (48)), while the next most active constraint was the one imposed on the first torsion reduced frequency k_{1t} ($g_4 \cong 0.1$) (Eq. (46)). Interestingly, the g_j values shown in Tables 6 and 7 confirm that the more passive constraints were: (i) the twist-flex coupling in the first flex frequency mode ζ_{1t-f} ($g_5 \geq 0.5$) (Eq. (47)), and (ii) the first-ply failure steady stress criterion σ_{failure} ($g_7 \geq 0.5$) (Eq. (49)) of the 32-ply blade due to the steady centrifugal tensile and gas flow-induced bending loads.

Shown also in the last rows of Tables 6 and 7 are cost functions and design constraints of the assumed off-design fan stiffness shown in the last rows of Tables 8 and 9. Shown therein are the fan stiffnesses, as the angle-ply orientations θ_i were rounded to nearest 5 deg about the optimum $\theta_{i_{\text{opt}}}$, which were very close to the optimum fan designs. All constraints remained passive in the off-design analysis and the cost functions were only 0.5% away from the corresponding ROS and Newsumt-A [3] optimum designs of the 16-ply and 32-ply fans. These off-design findings suggest that an assumed manufacturing tolerance of ±5 deg angle-ply orientation from the present optimum fan designs had very little effect on the optimality of the fan stiffness tailoring (i.e., satisfaction of the objective function and all constraints).

In Tables 8 and 9 are the optimum design histories of the fan stiffness (angle-ply orientations) of the 16-ply and 32-ply baseline fans operating at the design wheel speed Ω. As indicated in Tables 8 and 9, the most outer surface layer of the 16-ply and 32-ply fan blades were prescribed and remained 0 deg along the entire optimization process to carry at least a minimum amount of centrifugal tensile stresses near the hub of the fan. Each row of the tables presents the angle-ply orientations for a redesign surface from the baseline to optimum design. Although not shown in Tables 6(*a*), 7(*a*), 8(*a*), and 9(*a*), the iteration history of the fan stiffness and shape converged along the design constraint boundaries oscillating back and forth both slightly inside and outside the feasible design space to the optimum point, as illustrated in Fig. 8. By contrast one can see in Tables 6(*b*), 7(*b*), 8(*b*), and 9(*b*), the Newsumt-A [3] iteration history of the angle-ply orientations funneled inside the feasible design space to the optimum design point (as shown in Fig. 8), and the optimum fan designs are approximately divided to three groups of fan stiffness (i.e., angle-ply orientations of ±10 deg, ±60 deg, and ±90 deg). These results suggest that the optimum fan stiffness designs are reasonably sufficient for principle normal stress resistance to centrifugal tension

Table 8 (*a*) ROS and (*b*) Newsumt-A [3] optimum design of fan stiffness (angle-ply orientations, θ_t, in deg) and fan shape (m_T, in deg) for the 16-ply composite bypass fan operating at the design wheel speed Ω ([0 deg, +45 deg, 0 deg$_2$, −45 deg$_5$]$_s$ ply-orientation (subscripted numbers denote ply-layers) of 0.098 in. (0.249 cm) ply-thickness)

Design surface	θ_0[a]	θ_1	θ_2	θ_3	θ_4	θ_5	θ_6	θ_7	θ_8	m_T
(a) Baseline	0.0	45.0	0.0	0.0	−45.0	−45.0	−45.0	−45.0	−45.0	−26.6
Optimum	**0.0**	**45.0**	**0.0**	**−45.0**	**−70.5**	**−71.7**	**−74.8**	**−50.6**	**−8.0**	**−20.0**
Rounded[b]	0.0	45.0	0.0	−45.0	−70.0	−70.0	−75.0	−50.0	−10.0	
(b) Baseline	0.0	45.0	0.0	0.0	−45.0	−45.0	−45.0	−45.0	−45.0	−26.6
1	0.0	30.4	26.0	15.9	−13.8	−43.2	−53.3	−36.0	−2.3	−26.9
2	0.0	33.7	29.8	19.2	−15.4	−48.3	−47.0	−43.7	−8.0	−26.5
3	0.0	38.9	32.4	14.8	−11.5	−51.3	−53.1	−49.0	−8.1	−27.1
4	0.0	42.8	29.4	14.4	−10.6	−53.6	−52.3	−49.6	−5.8	−27.5
5	0.0	43.9	29.1	14.4	−9.8	−50.2	−51.9	−50.1	−5.6	−27.5
Optimum	**0.0**	**43.9**	**29.1**	**14.4**	**−9.8**	**−50.2**	**−51.9**	**−50.1**	**−5.6**	**−27.5**
Rounded[b]	0.0	45.0	30.0	15.0	−10.0	−50.0	−50.0	−50.0	−5.0	

[a]Prescribed 0 deg plies oriented to carry fan centrifugal stresses near hub.
[b]Fan design as optimized fan stiffness (angle-ply orientations) are rounded to nearest 5 deg.

Table 9 (*a*) ROS and (*b*) Newsumt-A [3] optimum design of fan stiffness (angle-ply orientations, θ_i, in deg) and fan shape (m_T, in deg) for the 32-ply composite bypass fan operating at the design wheel speed Ω ([0 deg$_2$, +45 deg$_2$, 0 deg$_4$, −45 deg$_{10}$]$_s$ ply-orientation (subscripted numbers denote ply-layers) of 0.049 in. (0.1245 cm) ply-thickness)

Design surface	θ_0[a]	θ_1	θ_2	θ_3	θ_4	θ_5	θ_6	θ_7	θ_8
(a) Baseline	0.0	45.0	45.0	0.0	0.0	0.0	0.0	−45.0	−45.0
Optimum	**0.0**	**−42.2**	**2.8**	**−42.2**	**−3.0**	**42.0**	**60.2**	**50.1**	**45.8**
Rounded[b]	0.0	−40.0	5.0	−40.0	−5.0	40.0	60.0	50.0	45.0
Design surface	θ_9	θ_{10}	θ_{11}	θ_{12}	θ_{13}	θ_{14}	θ_{15}	θ_{16}	m_T
Baseline	−45.0	−45.0	−45.0	−45.0	−45.0	−45.0	−45.0	−45.0	−26.6
Optimum	**22.8**	**−22.2**	**−60.1**	**−64.0**	**−86.8**	**−89.0**	**−44.6**	**−1.3**	**−20.0**
Rounded[b]	25.0	−20.0	−60.0	−65.0	−85.0	−90.0	−45.0	0.0	
Design surface	θ_0[a]	θ_1	θ_2	θ_3	θ_4	θ_5	θ_6	θ_7	θ_8
(b) Baseline	0.0	45.0	45.0	0.0	0.0	0.0	0.0	−45.0	−45.0
1	0.0	35.1	42.6	8.6	30.4	28.0	3.7	−31.5	−48.2
2	0.0	34.0	45.2	23.4	25.4	20.2	7.6	−19.2	−51.7
3	0.0	39.3	49.0	31.5	27.8	21.7	10.8	−13.7	−49.5
4	0.0	42.8	48.2	42.2	26.7	18.9	9.8	−12.7	−50.0
5	0.0	43.4	48.3	45.4	23.9	17.3	9.5	−11.8	−50.5
Optimum	**0.0**	**43.8**	**51.7**	**46.7**	**23.6**	**16.5**	**8.1**	**−11.8**	**−51.3**
Rounded[b]	0.0	45.0	50.0	45.0	25.0	15.0	10.0	−10.0	−50.0
Design surface	θ_9	θ_{10}	θ_{11}	θ_{12}	θ_{13}	θ_{14}	θ_{15}	θ_{16}	m_T
Baseline	−45.0	−45.0	−45.0	−45.0	−45.0	−45.0	−45.0	−45.0	−26.6
1	−47.9	−44.7	−57.2	−44.8	−48.3	−21.0	−4.2	7.1	−28.6
2	−48.7	−51.0	−51.4	−49.8	−49.5	−28.3	−5.6	6.8	−32.7
3	−42.2	−47.6	−50.2	−49.7	−49.6	−29.1	−6.8	7.0	−29.4
4	−41.6	−47.0	−50.0	−49.6	−49.5	−29.0	−6.1	7.3	−27.7
5	−46.8	−46.8	−49.9	−49.7	−49.7	−27.9	−5.0	7.7	−27.6
Optimum	**−47.6**	**−47.1**	**−50.1**	**−49.9**	**−49.9**	**−27.7**	**−4.6**	**7.7**	**−27.5**
Rounded[b]	−50.0	−45.0	−50.0	−50.0	−50.0	−30.0	−5.0	10.0	

[a]Prescribed 0 deg plies oriented to carry fan centrifugal stresses near hub.
[b]Fan design as optimized fan stiffness (angle-ply orientations) are rounded to nearest 5 deg.

with angle-ply orientations from –10 deg to +10 deg, for principle shear stress resistance to torsion with angle-ply orientations around ±60 deg, and for bird strike resistance with ±90 deg angle-ply orientations.

As depicted in Figs. 1 and 2, the thickness ratio of the fan (i.e., h/b) was fixed as 15% at the dovetail and 2% at the tip for the entire optimization process. The thickness tuning variable m_T was used for the fan mass-balancing (shape) optimization, which determined the slope of the thickness distribution of the fan blades primarily from the dovetail to approximately the mean radial height. The m_T of baseline composite fan was set to –26.6 deg and the range of m_T was limited by the side constraint –70 deg $< m_T <$ –20 deg (Eq. (63)). Smaller values of m_T imply a thinner, more mass-balanced fan. The iteration histories leading to the optimum thickness tuning variable m_T are shown in the last column of Tables 8 and 9. For instance, in Tables 8*a* and 9*a*, the ROME optimization findings reveal the shape parameter m_T decreases from a baseline fan shape design of –26.6 deg to an optimum fan shape design of –20 deg, implying *thinner less stiff, yet more mass-balanced* 16-ply and 32-ply fans, and relying on *more passive (less sensitive, Fig. 3) control* of fan stiffness from optimized angle-ply orientations $\theta_{i_{opt}}$ in satisfying the design constraints (Eqs. (54)–(63)). By contrast in Tables 8(*b*) and 9(*b*), the Newsumt-A [3] optimization findings reveal the shape parameter m_T increases from a baseline fan shape design of –26.6 deg to an optimum fan shape design of –27.5 deg, implying *thicker more stiff, yet less mass-balanced* 16-ply and 32-ply fans, and relying on *less passive* (*more sensitive, Fig. 3) control* of fan stiffness from optimized angle-ply orientations $\theta_{i_{opt}}$ in satisfying the design constraints.

As stated previously, the necessary conditions for a local or global minimum at a design point (θ_i^*, m_T^*) are that there exists a set of $\lambda_j^* \geq 0$ that satisfies the Kuhn–Tucker conditions [25,37,65–71]—the system of simultaneous nonlinear partial differential equations the ROS design synthesis technology (Eqs. (55)–(57), (63)–(73)) explicitly and directly solved in this work. The solution of Eqs. (55)–(57) and (63)–(73) establishes the design θ_i and m_T that minimizes $H(\theta_i, m_T)$ (Eq. (42)) subjected to constraints $g_j(\theta_i, m_T) \geq 0$ (Eqs. (43)–(50)), and side constraints $-\pi/2 = \theta^{(L)} \leq \theta_i \leq \theta^{(U)} = \pi/2$ (Eq. (51)] and -70 deg $\leq m_T \leq -20$ deg (Eq. (52)). As the objective function $H(\theta_i, m_T)$ (Eq. (42)) is convex and the constraints $g_j(\theta_i, m_T) \geq 0$ (Eqs. (43)–(50)), and side constraints $-\pi/2 = \theta^{(L)} \leq \theta_i \leq \theta^{(U)} = \pi/2$ (Eq. (51)) and -70 deg $\leq m_T \leq -20$ deg (Eq. (52)) are concave functions, the convex feasible region (as Eqs. (53) and (54) were satisfied) contained no relative local optima or saddle points, and the satisfaction of the Kuhn–Tucker conditions were necessary and sufficient for a global optimum. Otherwise, when the feasible region is not convex, then the Kuhn–Tucker conditions are necessary, if a design point is to be a relative local optimum. It should be stated that in using the Newsumt-A [3] benchmark software package, it may be difficult in some instances to ascertain a priori convexity of the nonlinear objective and constraint functions, which are typically used in turbomachinery fan design. Such a determination of convexity (Eqs. (53) and (54)) a priori is not required in employing the present ROS technology. Even if a properly formulated fan design problem is not convex, a global optimum may indeed exist. Or, a sequence of improved fan designs may be obtained from the redesign history yielding a reasonably converged relative local optimum solution.

The necessary and sufficiency conditions of Kuhn–Tucker optimality [25,37,65–71] (Eqs. (55)–(57)) for the present ROS and Newsumt-A [3] optimum designs is shown in Tables 10 and 11 for the 16-ply and 32-ply fans, respectively. Listed herein are the design constraints (Eqs. (43)–(52)) and their corresponding Lagrange multipliers, which is a ratio of the objective function, $H(\theta_i, m_T)$ sensitivity with respect to the design variables (θ_i, m_T) to

Table 10 Kuhn–Tucker conditions for (*a*) ROS and (*b*) Newsumt-A [3] optimized 16-ply composite bypass fan ([0 deg, +45 deg, 0 deg_2, −45 deg_5]$_s$ ply-orientation (subscripted numbers denote ply-layers) of 0.098 in. (0.249 cm) ply-thickness)

j	1	2	3	4	5	6	7	8
g_j	0.1	0.1	0.1	0	0.5	0	1	1
λ_j	0	0	0	330.9	0	390.6	0	0
j	9	10	11	12	13	14	$\nabla f_{,i} + \lambda_j \nabla g_{j,i}$	
g_j	1	1	0.6	0	0.1	0.5		
λ_j	0	0	0	0	0	0	0	
j	1	2	3	4	5	6	7	8
g_j	0.1	0.1	0.2	0	0.5	0	0.7	0.7
λ_j[a]	0	0	0	180.6	0	0	0	0
j	9	10	11	12	13	14	$\nabla f_{,i} + \lambda_j \nabla g_{j,i}$	
g_j	0.5	0.1	1	1	0	0		
λ_j[a]	0	0	0	0	0	0	0[a]	

[a]λ_j were calculated outside Newsumt-A by assuming the Kuhn–Tucker conditions were satisfied.

the constraint functions $g_j(\theta_i, m_T)$ sensitivity with respect to the design variables (θ_i, m_T). In Tables 10(*b*) and 11(*b*) the Lagrange multipliers λ_j were calculated outside Newsumt-A [3] by assuming the Kuhn–Tucker optimality conditions (Eqs. (55)–(57)) were satisfied, since such conditions are neither explicitly nor directly determined in the sequential unconstrained minimization technique employed inside the Newsumt-A software package [3].

As can be seen in Tables 10 and 11, all constraints at the optimum solution are $g_j^*(\theta_i^*, m_T^*) > 0$, all Lagrange multipliers at the optimum solution are $\lambda_j^* \geq 0$, and Eq. (57) are satisfied (as zero) for both the 16-ply and 32-ply fans at the present optimum design solutions. Since the Kuhn–Tucker optimality conditions were explicitly and directly determined using the present ROS technology, the ROS optimum fan designs achieved were indeed

Table 11 Kuhn–Tucker conditions for (*a*) ROS and (*b*) Newsumt-A [3] optimized 32-ply composite bypass fan ([0 deg_2, +45 deg_2, 0 deg_4, −45 deg_{10}]$_s$ ply-orientation (subscripted numbers denote ply-layers) of 0.049 in. (0.1245 cm) ply-thickness)

j	1	2	3	4	5	6	7	8
g_j	0.1	0.1	0.1	0	0.5	0	0.9	0.9
λ_j	0	0	0	4.1	0	5.8	0	0
j	9	10	11	12	13	14	15	16
g_j	1	1	0.9	1	0.4	0.2	0.1	0.5
λ_j	0	0	0	0	0	0	0	0
j	17	18	19	20	21	22	$\nabla f_{,i} + \lambda_j \nabla g_{j,i}$	
g_j	1	0.8	0.1	0.5	0.1	1		
λ_j	0	0	0	0	0	0	0	
j	1	2	3	4	5	6	7	8
g_j	0.1	0.1	0.1	0.1	0.4	0	0.8	0.9
λ_j[a]	0	0	0	180.6	0	0	0	0
j	9	10	11	12	13	14	15	16
g_j	0.5	0.8	0.8	0.6	0.1	0.9	1	0.9
λ_j[a]	0	0	0	0	0	0	0	0
j	17	18	19	20	21	22	$\nabla f_{,i} + \lambda_j \nabla g_{j,i}$	
g_j	1	1	0.5	0.5	0.7	0		
λ_j[a]	0	0	0	0	0	0	0[a]	

[a]λ_j were calculated outside Newsumt-A [3] by assuming the Kuhn–Tucker conditions were satisfied.

global optimum solutions. In addition, assuming the Kuhn–Tucker conditions were satisfied as shown in Tables 10(*b*) and 11(*b*), a powerful test of goodness of optimality was provided for the local optimum design solutions predicted by the general-purpose Newsumt-A software package [3]. Furthermore, the theoretical finding of Eqs. (57) and (62) suggests to fan designers a definitive numerical strategy for quantitative ROS solution assessments (Tables 10(*a*) and 11(*a*)) and qualitative Newsumt-A [3] solution assessments (Tables 10(*b*) and 11(*b*)) of optimum fan stiffness and shape designs for tailored vibration response and flutter control.

Shown in Fig. 9 are the Campbell diagrams of the 16-ply and 32-ply ROS and Newsumt-A [3] optimized fans. Frequency curves are displayed for the baseline composite fan (shown in dashed) and the ROS and Newsumt-A [3] optimized fans (shown as a normal line (for the 16-ply fan) and as a bold line (for the 32-ply fan)). Also indicated on the Campbell diagrams is the normal operating range of the engine fan, which is bracketed by the vertical dashed lines at the 50%Ω and 75%Ω off-design wheel speeds and the 100% design wheel speed Ω.

It can be seen in the Fig. 9 that the first flex (1B) mode of the baseline blade has 2 per rev and 3 per rev crossing below 50%Ω (low engine speed) and the second flex (2B) mode crosses 3 per rev around 72%Ω, which might be judged somewhat less critical. And, the coupled first torsion (1T) mode crosses the 4 per rev at approximately 85%Ω, which might present extremely critical blade pitching during a typical takeoff condition, and thus could not be tolerated.

Comparing the tailored vibration response and flutter control performance of the present newly developed ROS and general-purpose Newsumt-A [3] design synthesis (optimization) processes, the restructured Campbell diagrams (Fig. 9) of the combined optimized stiffness (16-ply and 32-ply) and optimized mass-balanced (tailored shaped) fans exhibit remarkably close agreement, more so in the lower first and second flex modes than the higher first torsion, third flex (3B), and fifth (first chordwise bending, 1CB) modes. It is concluded herein that the restructured ROS Campbell diagram is more accurate than the Newsumt-A Campbell diagram, because the present ROS design synthesis technology explicitly and directly solved the necessary and sufficient Kuhn–Tucker optimality conditions (Eqs. (55)–(57), (63)–(73)) for a global optimum fan design, although the general-purpose Newsumt-A software [3] does predict and benchmark a remarkably close local optimum fan design to the ROS one, as one can comparably see in Tables 6–11.

Several observations can be made about the restructured Campbell diagrams of Fig. 9. The coupled first flex mode (ω_{1f}) of the optimized fan has a 2 per rev crossing about 40%Ω, and the coupled second flex mode of the optimized fan has a 3 per rev crossing right below 75%W [$w_{2f,75\%\Omega} < 3E$]. Such critical speeds can be accelerated through rapidly without significant fan damage during engine start-up or shut-down. The coupled first torsion mode of the optimized fan is sufficiently higher than the lower order (1–4 per rev) critical speed within the normal operation range. More important, the separation within the normal operation range between the coupled second flex (ω_{2f}) and first torsion (ω_{1t}) modes of the optimized fans is substantially wider (by about 30 Hz) than that of the baseline fan design. This has been achieved, while at the same time, increasing the ω_{1t} and k_{1t} in the optimized fan from the infeasible region to the desired feasible region (see Tables 6 and 7). For the present optimized fans there is no critical speed for all modes at lower order engine speed (1–4 per rev) within the normal operation range (from 75%Ω to 100%Ω).

The 16-ply fan stiffness had available to it less variability than the 32-ply fan stiffness, because of the additional design variables used in both the present ROS design synthesis and the Newsumt-A [3] design. Nevertheless, as the number of design variables increased, the importance of explicitly solving the necessary and sufficiency Kuhn–Tucker conditions, as was developed inside the

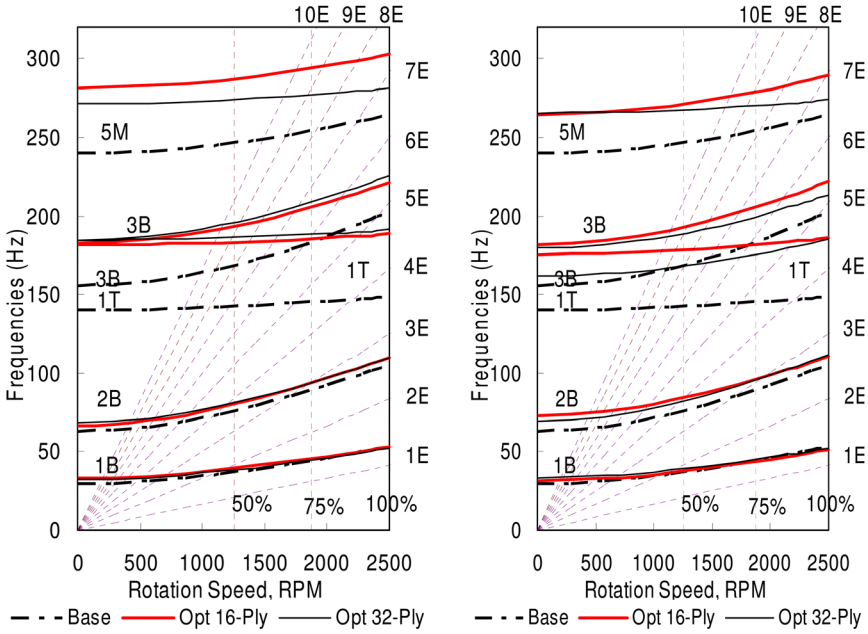

Fig. 9 Campbell diagrams of baseline fan and Newsumt-A [3] and ROS optimized 16-ply and 32-ply composite bypass fans ($[0\ \text{deg}, +45\ \text{deg}, 0\ \text{deg}_2, -45\ \text{deg}_5]_s$ (subscripted numbers denote ply-layers) 16-ply baseline fan orientation of 0.098 in. (0.249 cm) ply-thicknesses; $[0\ \text{deg}_2, +45\ \text{deg}_2, 0\ \text{deg}_4, -45\ \text{deg}_{10}]_s$ 32-ply baseline fan orientation of 0.049 in. (0.1245 cm) ply-thicknesses) (notation: "base" = baseline composite bypass fan; "opt 16-ply" = optimized 16-ply composite bypass fan; "opt 32-ply" = optimized 32-ply composite bypass fan)

Table 12 Summary of computational cost of fan optimization[a]

	ROS[b] 16-ply[c]	ROS[b] 16-ply[d]	ROS[b] 32-ply[c]	ROS[b] 32-ply[d]	FEM[d]
Baseline fan response (min)	1	1	2	2	2 (est.)
Updated fan response (s)	10	10	11	11	
Newsumt-A [3] software (h)	2.3	1.5	4	2.5	2 (est.)
Reanalyses (10^3)	1	0.5	1.5	0.8	

[a]Running time of the parallelized code on a SGI2000 origin with two processors (195 MHz for each processor). ROS design synthesis technology running time on a standard (3.2 GHz processors) desktop personal computer was 1.4 h (for ROS[e] 16-Ply[f]) and 5.5 h (for ROS[e] 32-Ply[f]).
[b]100-term 3D ROME response solutions [1,2] are used for Newsumt-A [3] optimization analysis.
[c]Newsumt-A [3] optimization with shape thickness tuning variable.
[d]Newsumt-A [3] optimization with constant shape thickness tuning variable.
[e]100-term 3D ROME response solutions are used for the ROS design synthesis technology.
[f]ROS design synthesis technology with shape thickness tuning variable.

present ROS technology, but not inside the general-purpose Newsumt-A software package [3], significantly impacted the design synthesis findings and the restructured Campbell diagrams shown in Fig. 9. It is interesting in Fig. 9 that the Newsumt-A [3] design predicted slightly *less* stiff 1B, 2B, 1T, and 3B modes of the optimum 16-ply fan than the optimum 32-ply fan. In contrast, the present ROS design predicted opposite outcomes, correctly showing slightly stiffer 1B, 2B, 1T, and 3B modes of the optimum 16-ply fan than the optimum 32-ply fan. The restructuring of the fifth (1CB) (ω_{1CB}) mode is more absolute between the Newsumt-A [3] design prediction and the present ROS one. The differences between the Newsumt-A [3] and present ROS restructured Campbell diagrams of Fig. 9, albeit small, do exhibit an essential finding of this work of the power of the accurate and direct solutions achieved using ROS technology for the simultaneous nonlinear partial differential equations characterizing the Kuhn–Tucker optimality conditions (Eqs. (55)–(57)) for the global optimum fan design.

A few words regarding the computational efficiency of the newly developed ROS and 3D ROME technology is fitting. Summarized in Table 12 is the computational cost of the baseline fan stiffness and shape optimization. The CPU time is measured on a digital Alpha-Station 500/266. There are two types of analysis in the optimization process using 3D ROME free vibration response modeling [1,2], which are indicated in Table 12 as the baseline fan analysis and each updated fan analysis. The baseline fan analysis is executed while the mass-balancing distribution changed with an updated shape (thickness) tuning variable m_T, appropriately determined at each new optimization surface. Because the mass (volume) of fan changed by the thickness distribution a new reevaluation of the fan volume was required to construct the 3D ROME response system matrices. The shape (thickness) tuning variable m_T remained unchanged in determining a new optimization surface and the passive stiffness (angle-ply orientations θ_i) variables were the only variables redetermined in the optimization analyses. Since, in this case, only the material matrix needed to be

Table 13 Off-design fan stiffness sensitivity analysis of ROS[a] (left) and Newsumt-A [3][b] (right) optimized 16-ply and 32-ply composite bypass fans ([0 deg, +45 deg, 0 deg$_2$, −45 deg$_5$]$_s$ 16-ply baseline fan orientation (subscripted numbers denote ply-layers) of 0.098 in. (0.249 cm) ply-thicknesses; [0 deg$_2$, +45 deg$_2$, 0 deg$_4$, −45 deg$_{10}$]$_s$ 32-ply baseline fan orientation of 0.049 in. (0.1245 cm) ply-thicknesses)

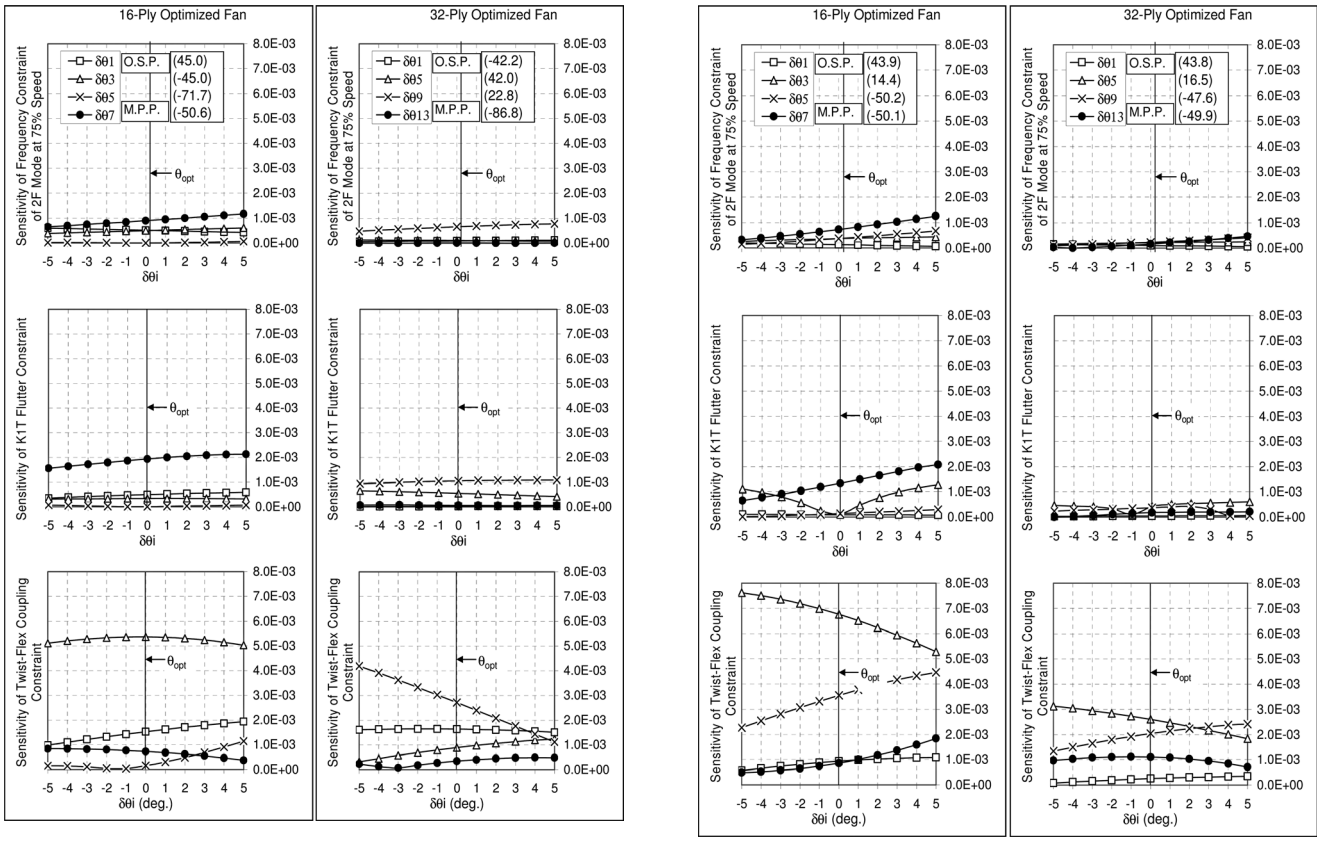

[a]ROS: M.P.P. = midplane plies; O.S.P. = outer surface plies ($\delta\theta_i = \pm 5$ deg, relative to ROS optimum solutions ($\theta_{1opt} = +45$ deg, $\theta_{3opt} = -45$ deg, $\theta_{5opt} = -71.7$ deg, $\theta_{7opt} = -50.6$ deg, for the 16-ply optimized fan; $\theta_{1opt} = -42.2$ deg, $\theta_{5opt} = +42$ deg, $\theta_{9opt} = +22.8$ deg, $\theta_{13opt} = -86.8$ deg, for the 32-ply optimized fan).

[b]Newsumt-A: M.P.P. = midplane plies; O.S.P. = outer surface plies ($\delta\theta_i = \pm 5$ deg, relative to Newsumt-A [3] optimum solutions ($\theta_{1opt} = +43.9$ deg, $\theta_{3opt} = +14.4$ deg, $\theta_{5opt} = -50.2$ deg, $\theta_{7opt} = -50.1$ deg, for the 16-ply optimized fan; $\theta_{1opt} = +43.8$ deg, $\theta_{5opt} = +16.5$ deg, $\theta_{9opt} = -47.6$ deg, $\theta_{13opt} = -49.9$ deg, for the 32-ply optimized fan).

revised, the 3D ROME reanalysis was executed with less cost by using the system matrices stored from the previous analysis and optimization surface.

The computational cost of the optimization analysis for the 16-ply and 32-ply optimized fans are listed in the Table 12. As can be seen in Table 12, the running times of the general-purpose Newsumt-A [3] fan stiffness and shape optimization was 2.3 h for the 16-ply fan and 4 h for the 32-ply fan. As the mass-balancing or shape (thickness) tuning variable m_T was held fixed, the cost of the Newsumt-A [3] optimization was reduced to 1.5 h for the 16-ply fan and 2.5 h for the 32-ply fan. The latter reduced running times was achieved by executing significantly cost-efficient 3D ROME updated fan response reanalyses that only updated the material constants matrix inside the dynamical system matrix of the baseline fan. More important, the ROS fan stiffness and shape optimization was cost-efficient enough to be performed on a standard (3.2 GHz processor) desktop personal computer. As indicated in Table 12, the desktop personal computing running times of the complete ROS fan stiffness and shape optimization was 1.4 h for the 16-ply fan and 5.5 h for the 32-ply fan.

9 Off-Design Sensitivity of the Optimized Composite Fan

Table 13 shows the off-design sensitivity with respect to the most active constraints associated with the present tailored vibration response and flutter control through fan stiffness and mass-balancing (shape) optimization. The $\delta\theta_i$ (horizontal axis) is the variation (off-design) of the fan stiffness (showing considerable tolerance of angle-ply orientations, $\delta\theta_i$ from −5 deg to +5 deg) about the optimized fan (indicated in Table 13 as θ_{opt}). The left side of Table 13 charts off-design fan stiffness sensitivity findings of the ROS optimized 16-ply and 32-ply composite bypass fans, having $\delta\theta_i = \pm 5$ deg, relative to the ROS optimum solutions ($\theta_{1opt} = +45$ deg, $\theta_{3opt} = -45$ deg, $\theta_{5opt} = -71.7$ deg, $\theta_{7opt} = -50.6$ deg, for the 16-ply optimized fan; $\theta_{1opt} = -42.2$ deg, $\theta_{5opt} = +42$ deg, $\theta_{9opt} = +22.8$ deg, $\theta_{13opt} = -86.8$ deg, for the 32-ply optimized fan). In contrast, the right side of Table 13 charts off-design fan stiffness sensitivity findings of the Newsumt-A [3] optimized 16-ply and 32-ply composite bypass fans, having $\delta\theta_i = \pm 5$ deg, relative to the Newsumt-A [3] optimum solutions ($\theta_{1opt} = +43.9$ deg, $\theta_{3opt} = +14.4$ deg, $\theta_{5opt} = -50.2$ deg, $\theta_{7opt} = -50.1$ deg, for the 16-ply optimized fan; $\theta_{1opt} = +43.8$ deg, $\theta_{5opt} = +16.5$ deg, $\theta_{9opt} = -47.6$ deg, $\theta_{13opt} = -49.9$ deg, for the 32-ply optimized fan). The off-design sensitivity for constraints $S(g_j)$ (vertical axis) is actually the gradient of the constraints measured at the given off-design $\delta\theta_i$ points using a simple central-difference approximation, as follows:

$$S(g_j) = \frac{[g_j(\theta_{\text{opt},i} + \delta\theta_i + 0.01) - g_j(\theta_{\text{opt},i} + \delta\theta_i - 0.01)]}{0.02} \quad (75)$$

Four selected plies of the optimized fan stiffness were examined, i.e., layers 1, 3, 5, and 7 of the 16-ply composite fan and layers 1,

5, 9, and 13 of the 32-ply composite fan. Indicated also in Table 13 are the notations O.S.P., which denotes the "outer-surface ply," selected as layer 1, and M.P.P., which denotes the "midplane ply," selected as layer 7 for the 16-ply composite fan and layer 13 for the 32-ply composite fan. The off-design sensitivities shown therein are for the constraints, first torsion reduced frequency, $k_{1t} > 0.7$ (Eq. (44)), second flex frequency, $\omega_{2f,75\%} < 3E = 3\Omega$ (Eq. (46)), and the twist-flex coupling in the first flex mode, $\zeta_{1t-f} = b\alpha/(2\Delta_b) < 0.2$ (Eq. (45)).

One can see that all of the off-design sensitivities for constraints summarized in Table 13 were less than the order of 8×10^{-3}, which means the constraints were very insensitive to off-design, $\delta\theta_i = \pm 5$ deg, about the ROS and Newsumt-A [3] optimum design solutions indicated in Table 13. Specifically, the M.P.P. ($\delta\theta_7$ for the 16-ply composite fan and $\delta\theta_{13}$ for the 32-ply composite fan) were more sensitive fan stiffness controllers than the other plies in tailoring the second flex response, $\omega_{2f,75\%} < 3E = 3\Omega$ (Eq. (46)). The M.P.P. was thicker and stiffer in the optimized fans in contrast to the O.S.P., which was thinner, possessing less stiffness control. Hence, the thicker M.P.P. possessed more volume as a passive fan stiffness controller, carrying more vibration energy of the fans, and resulting in more second flex response sensitivity in the off-designs summarized in Table 13. It can be inferred that in Table 13 that the O.S.P. passive stiffness control was more sensitive to twist-flex coupling, $\zeta_{1t-f} = b\alpha/(2\Delta_b) < 0.2$ (Eq. (45)), whereas the M.P.P. passive stiffness control was more sensitive to first torsion flutter, $k_{1t} > 0.7$ (Eq. (44)). Generally speaking, the off-design analysis of the ROS and Newsumt-A [3] optimized fans exhibited little sensitivity of twist-flex coupling response, flutter and frequency constraints with respect to small errors known as angle-ply laminate construction misalignments [44–48] in optimum fan stiffness (angle-ply design construction).

10 Concluding Remarks

In the present work a new reduced-order, passive stiffness control and shape optimization technology has been developed for tailored vibration response and flutter protection of high-bypass, shroudless fans. A newly developed integrated three-dimensional reduced-order spectral-based energy composite fan free response [1,2] and a novel reduced-order spectral-based nonlinear constrained minimization design synthesis technology has been proposed herein to passively tune the fan stiffness through an optimum selection of angle-ply orientations and fan mass-balanced shape through a dovetail-to-midradial height thickness redistribution, while at the same time, preserving the fan's basic aerodynamic profile characteristics. The developed 3D reduced-order spectral-based meshless energy technology of mechanical response of the baseline composite fan is shown to be highly cost effective and accurate, when its predictive free response capability is compared to general-purpose finite element technology widely used by industry. The convergence accuracy and solution error of the present 3D reduced-order spectral-based meshless energy method can be regarded as estimated, both completely and theoretically, in that the exact solution to the baseline fan vibrations must lie well inside a 1% bandwidth between the converged perfectly restrained upper-bound and imperfectly restrained lower, upper-bound 3D solutions (Tables 2 and 3).

Coupled flex-torsion frequency data and Campbell diagrams for high-fidelity, reduced-order models of high-bypass fans summarize optimum design histories of fan stiffness (angle-ply orientations) and mass-balanced (blade shape) thickness distribution and nondimensional constraints, which alleviate integral order resonant and stall flutter characteristics, control twist-flex response mechanisms, and ensure the mechanical strength integrity of the fan under steady centrifugal tension and gas flow-induced bending stresses. Baseline and optimally restructured Campbell diagrams and design sensitivity calculations show that a proper implementation of stiffness tailoring and mass-balanced (shape) optimization of high-bypass fans produce feasible Campbell diagrams that satisfies all design goals. An off-design analysis of the optimum fan configuration shows little sensitivity of twist-flex coupling response and flutter design constraints with respect to small variability or errors in optimum design construction. Industry manufacturing processes may initiate these small errors or angle-ply laminate construction misalignments [44–48]. One can see that all of the off-design sensitivities for constraints summarized in Table 13 were less than the order of 8×10^{-3}, which means the constraints were very insensitive about the ROS and Newsumt-A [3] optimum design solutions obtained.

Subject to further numerical studies by structural dynamicists and aeroelasticians, the authors believe that a reasonably compelling integrated design synthesis explanation has been given to an open query that it is simultaneously advantageous to separate the critical lower twist-flex modes and to control the dynamic twist-flex mode coupling for response protection against integral order resonance and stall flutter of a specific class of cold-stream, transonic, high-bypass fans. Design constraints, such as mode separation, coupled mode response suppression, and empirical flutter data, have been simultaneously satisfied in the problem to produce sublaminate blade designs with proper resistance to centrifugal tension and to first angle-ply principal stress failure. It is also suggested that a proper selection of fan stiffness and mass-balanced shape can be made within the setting of an appropriate reduced-order spectral-based nonlinear constrained minimization technology.

To ensure the accuracy and global convergence quality of the reduced-order spectral-based nonlinear constrained minimization technology developed in this study for high-bypass fan design, analysts should consider a stationary solution of simultaneous nonlinear partial differential equations (in terms of the design variables (θ_i, m_T) and slack variables or Lagrange multipliers λ_j), determining the Kuhn–Tucker conditions of global optimality [25,37,65–71] (Eqs. (55)–(57)), which has been explicitly and directly solved using a new ROS design synthesis technology (Eqs. (63)–(73)). Solution accuracy of the reduced-order spectral-based design synthesis technology—presented for the first time in the open literature—has been compared against the general-purpose nonlinear mathematical programming software package Newsumt-A [3] (a widely used sequential unconstrained minimization technique, which does not explicitly solve the Kuhn–Tucker optimality conditions). Rather, in Newsumt-A [3], for small penalty factor r_p in Eqs. (74), finding the minimum of an augmented Lagrangian φ was equivalent to finding the stationary points of fan cost function $H(\theta_i, m_T)$. It has been confirmed from the reduced-order spectral-based design synthesis technology that the Kuhn–Tucker conditions [25,37,65–71] (that is, first-order stationary conditions of the associated augmented Lagrangian φ) are necessary and sufficient conditions of global optimality of solutions (as convexity Eqs. (53) and (54) are satisfied), and that they were completely satisfied at the reduced-order spectral-based global optimum fan design solutions, and acceptably satisfied at the Newsumt-A [3] local optimum fan design solutions obtained in this study.

The overall impact of this study increases aviation safety by supplementing current availability of enhanced design technologies that reduce the incidence of catastrophic accidents resulting from aircraft propulsion system component malfunctions. In particular, the present design strategy may lead to improved reliability of high-energy, rotating, cold-stream fan components in propulsion systems. The greater fan reliability proposed here results from tailored vibration response suppression and flutter instability control, leading to an optimum fan design of mechanical strength and shape that may alleviate high-cycle fatigue and uncontained engine failures.

Acknowledgment

This research was supported by the National Aeronautics and Space Administration (NASA) Faculty Award for Research

(FAR), Grant Number NAG3-1571, under technical monitor, Mr. John Lucero, Structural Dynamics Branch at the NASA Glenn Research Center. Additional support was provided by the National Science Foundation, Presidential Young Investigator (PYI) Program under NSF-CMS 9618308, the Department of Defense Army Research Office's Multidisciplinary Research Program of the University Research Initiative (MURI), by Pratt & Whitney, West Palm Beach, Florida under the technical monitoring of Dr. Yehia El-Aini, Senior Fellow, Aeromechanics, Structures & Dynamics, and finally, for the second author, by Ohio State University's Department of Civil and Environmental Engineering and Geodetic Science and College of Engineering, and by Howard University's Office of the Vice President for Research and Compliance. Portions of this paper were prepared while the first author was a Martin Luther King, Jr. Visiting Associate Professor in the MIT Department of Aeronautics and Astronautics, and the MIT Department of Civil and Environmental Engineering. Support from these departments and organizations are most gratefully acknowledged. The technical guidance and practical insight of Dr. Robert E. Kielb of the Department of Mechanical Engineering at Duke University and Dr. Eric Ducharme of the Blade Stress and Aeromechanics Group at GE Aircraft Engines, both of whom made valuable suggestions, which influenced the early-stage scope of the paper, cannot be overstated. The authors' gratitude to these teachers exceeds the realms of ordinary expressions. Finally, the authors wish to express their sincere appreciation to Professor Jiunn Fang of the Department of Aeronautical Engineering at Feng Chia University, Taiwan, for his helpful assistance with the ANSYS blade calculations and for the computational resources of the Dec3000 Alpha Station 500/266. Portion of this work was completed while the first author was supported as a National Aeronautics and Space Administration (NASA) Glenn Research Center Summer Faculty Fellow in Brookpark, Ohio USA. Additional portions of this work was sponsored by the Air Force Office of Scientific Research, United Technology Corporation Prime Contract Number FA8650–08-D-2806, Task Order 0004, and Howard University Subcontract Agreement 10-S590-0004-02-C16 under Jeff Brown, Government Technical Monitor, WPAFB AFRL/RZTS, Joseph Gordon, and Donnie Saunders, Government Task Order Monitors, AFRL/RZ, and Michele Puterbaugh, UTC Task Order Monitor. Support from these departments and organizations are most gratefully acknowledged.

References

[1] McGee, O. G., Fang, C., and El-Aini, Y., 2013, "A Reduced-Order Meshless Energy Model for the Vibrations of Mistuned Bladed Disks—Part I: Theoretical Basis," ASME J. Turbomach. (in press).
[2] Fang, C., McGee, O. G., and El-Aini, Y., 2013, "A Reduced-Order Meshless Energy Model for the Vibrations of Mistuned Bladed Disks—Part II: Finite Element Benchmark Comparisons," J. Turbomach. (in press).
[3] Miura, H., and Schmit, Jr., L. A., 1979, "NEWSUMT–A, Fortran Program For Inequality Constrained Function Minimization—Users Guide," NASA CR-159070.
[4] Campbell, W., 1924, "Protection of Steam Turbine Disk Wheels From Axial Vibration," ASME Spring Meeting, Cleveland, OH, Paper 1920.
[5] Fleeter, S., and Hoyniak, D., 1987, "Chordwise Spacing Aerodynamic Detuning for Unstalled Supersonic Flutter Stability Enhancement," J. Sound Vib., **115**(3), pp. 483–497.
[6] Sladojević, I., Sayma, A. I., and Imregun, M., 2007, "Influence of Stagger Angle Variation on Aerodynamic Damping and Frequency Shifts," ASME TURBO EXPO'07, Montreal, Canada, May 14–17, ASME Paper No. GT2007-28166.
[7] Kielb, R. E., Hall, K. C., and Miyakozawa, T., 2007, "The Effects of Unsteady Aerodynamic Asymmetric Perturbations on Flutter," ASME TURBO EXPO'07, Montreal, Canada, May 14–17, ASME Paper No. GT2007-27503.
[8] Miyakozawa, T., Kielb, R. E., and Hall, K.C., 2008, "The Effects of Aerodynamic Perturbations on Forced Response of Bladed Disks," ASME TURBO EXPO'08, Berlin, June 9–13, ASME Paper No. GT2008-50719.
[9] Ekici, K., Kielb, R. E., and Hall, K.C., 2008, "Aerodynamic Asymmetry Analysis of Unsteady Flows in Turbomachinery," ASME TURBO EXPO'08, Berlin, June 9–13, ASME Paper No. GT2008-51176.
[10] Sanders, A., 2005, "Nonsynchronous Vibration Due to a Flow-Induced Aerodynamic Instability in a Composite Fan Stator," ASME J. Turbomach., **127**, pp. 412–421.
[11] Spiker, M. A., Kielb, R. E., Hall, K. C., and Thomas, J.P., 2008, "Efficient Design Method for Non-Synchronous Vibrations Using Enforced Motion," ASME TURBO EXPO'08, Berlin, June 9–13, ASME Paper No. GT2008-50599.
[12] Vo, H. D., 2010, "Role of Tip Clearance Flow in Rotating Instabilities and Nonsynchronous Vibrations," J. Propul. Power, **26**(3), pp. 556–561.
[13] Crawley, E. F., 1979, "The Natural Modes of Graphite/Epoxy Cantilever Plates and Shells," J. Composite Mater., **13**, pp. 195–205.
[14] Caprino, G., and Crivelli-Visconti, I., 1982, "A Note on Specially-Orthotropic Laminates," J. Composite Mater., **16**, pp. 395–399.
[15] Gunnink, J. W., 1983, "Comment on a Note on Specially Orthotropic Laminates," J. Composite Mater., **17**, pp. 508–510.
[16] Chamis, C. C., 1975, "A Theory for Predicting Composite Laminate Warpage Resulting From Fabrication," Society of the Plastics Industry 30th Anniversary Technical Conference, Reinforced Plastics/Composites Institute, Washington, DC, February 4–7.
[17] Minich, M. D., and Chamis, C. C., 1975, "Analytical Displacements and Vibrations of Cantilevered Unsymmetric Fiber Composite Laminates," NASA TM X-71699.
[18] Schmit, Jr., L. A., and Farshi, B., 1973, "Optimum Laminate Design for Strength and Stiffness," Int. J. Numer. Methods Eng., **7**, pp. 519–536.
[19] Rao, S. S., and Singh, K., 1979, "Optimum Design of Laminates With Natural Frequency Constraints," J. Sound Vib., **67**(1), pp. 101–112.
[20] Rao, S. S., 1978, *Optimization: Theory and Applications*, Wiley Eastern Limited, New Delhi.
[21] Rao, S. S., 1975, "Optimum Design of Structures Under Shock and Vibration Environment," Shock Vib. Dig., **7**, pp. 61–70.
[22] Bert, C. W., 1977, "Optimal Design of Composite-Material Plate to Maximize Its Fundamental Frequency," J. Sound Vib., **50**(2), pp. 229–237.
[23] Olhoff, N., 1976, "A Survey of Optimal Design of Vibrating Structural Elements. Part I—Theory," Shock Vib. Dig., **8**, pp. 3–10.
[24] Kiusalaas, J., and Shaw, R. C. J., 1978, "An Algorithm for Optimal Structural Design With Frequency Constraints," Int. J. Numer. Methods Eng., **13**(2), pp. 283–295.
[25] Haftka, R. T., and Gurdal Z., 1991, *Elements of Structural Optimization*, 3rd ed., Kluwer Academic, London.
[26] Bladh, R., Castanier, M. P., and Pierre, C., 2001, "Component Mode-Based Reduced-Order Modeling Techniques for Mistuned Bladed Disks—Part I: Theoretical Models," ASME J. Eng. Gas Turbines Power, **123**(1), pp. 89–99.
[27] Shiau, T. N., and Chang, S. J., 1991, "Optimization of Rotating Blades With Dynamic Behavior Constraints," ASCE J. Aerosp. Eng., **4**, pp. 127–144.
[28] Lin, C. C., and Yu, A. J., 1991, "Optimum Weight Design of Composite Laminated Plates," Comput. Struct., **38**(5/6), pp. 581–587.
[29] Lim, S.-H., Bladh, R., Castanier, M. P., and Pierre, C., 2003, "A Compact, Generalized Component Mode Mistuning Representation for Modeling Bladed Disk Vibration," Proceeding of the 44th AIAA/ASME/ASCE/AHS/ASC Structures, Structural Dynamics, and Materials Conference and Exhibit, Norfolk, VA, April 7–10, AIAA Paper 2003-1545.
[30] Shiau, T. N., Yu, Y. D., and Kuo, C. P., 1993, "Optimum Design of Rotating Laminate Blade With Dynamic Behavior Constraints," ASME Paper No. 93-GT-268.
[31] Ottarsson, G. S., and Pierre, C., 1993, "A Transfer Matrix Approach to Vibration Localization in Mistuned Blade Assemblies," ASME Paper No. 93-GT-115.
[32] Ottarsson, G. S., 1994, "Dynamic Modeling and Vibration Analysis of Mistuned Bladed Disks," Ph.D. thesis, University of Michigan, Ann Arbor, MI.
[33] Ottarsson, G. S., Castanier, M. P., and Pierre, C., 1994, "A Reduced-Order Modeling Technique for Mistuned Bladed Disks," AIAA-94-1640-CP, pp. 2552–2562.
[34] Yang, M.-T., and Griffin, J. H., 1997, "A Normalized Modal Eigenvalue Approach for Resolving Modal Interaction," ASME J. Eng. Gas Turbines Power, **119**, pp. 647–650.
[35] Yang, M.-T., and Griffin, J. H., 2001, "A Reduced-Order Model of Mistuning Using a Subset of Nominal System Modes," ASME J. Eng. Gas Turbines Power, **123**, pp. 893–900.
[36] Kenyon, J. A., and Griffin, J. H., 2003, "Forced Response of Turbine Engine Bladed Disks and Sensitivity to Harmonic Mistuning," ASME J. Eng. Gas Turbines Power, **125**, pp. 113–120.
[37] Kuhn, H. W., and Tucker, A. W., 1951, "Nonlinear Programming," Proceedings of the 2nd Berkeley Symposium on Mathematical Statistics and Probability, Berkeley, CA, July 31–August 12, 1950, University of California Press, Berkeley, pp. 481–492.
[38] Golub, G. H., and VanLoan, C. F., 1996, *Matrix Computation*, The John Hopkins University Press, Baltimore, MD.
[39] Kantorovich, L. V., and Krylov, V. I., 1958, *Approximate Methods of Higher Analysis*, P. Noordhoff, Ltd., Groningen, The Netherlands, English translation.
[40] Chakraverty, S., Bhat, R. B., and Stiharu, I., 1999, "Recent Research on Vibration of Structures Using Boundary Characteristic Orthogonal Polynomials in the Rayleigh-Ritz Method," Shock Vib. Dig., **31**(3), pp. 187–194.
[41] Jones, R. M., 1975, *Mechanics of Composite Materials*, McGraw-Hill, New York.
[42] McGee, O. G., and Chu, H. R., 1994, "Three-Dimensional Vibration Analysis of Rotating Laminated Composite Blades," ASME J. Eng. Gas Turbine Eng. Power, **116**(3), pp. 663–671.
[43] Cohen, H., Rogers, G. F. C., and Saravanamuttoo, H. I. H., 1987, *Gas Turbine Theory*, 3rd ed., Longman Scientific and Technical, Essex, UK, Chaps. 5 and 7.
[44] Graham, R. W., and Guentert, E. C., 1965, "Compressor Stall and Blade Vibration," Aerodynamic Design of Axial-Flow Compressors, NASA SP-36, Chap. XI.

[45] Meher-Hornji, C. B., 1995, "Blading Vibration and Failures in Gas Turbines, Part A: Blading Dynamics and the Operating Environment," ASME Paper No. 95-GT-418.
[46] Petrov, E. P., Sanliturk, K. Y., and Ewins, D. J., 2002, "A New Method for Dynamic Analysis of Mistuned Bladed Disks Based on the Exact Relationship Between Tuned and Mistuned Systems," ASME J. Eng. Gas Turbines Power, **124**(3), pp. 586–597.
[47] Wei, S. T., and Pierre, C., 1990, "Statistical Analysis of the Forced Response of Mistuned Cyclic Assemblies," AIAA J., **28**(5), pp. 861–868.
[48] Wisler, D. C., 1988, Advanced Compressor and Fan Systems, GE Aircraft Engines, Cincinnati, OH, Copyright 1988 by General Electric Co. All Rights Reserved (also 1986 Lecture to ASME Turbomachinery Institute, Ames IO).
[49] Lee, S. M. 1990, *International Encyclopedia of Composites*, Vol. 5, Wiley-VCH Verlag GmbH, Weinheim, Germany.
[50] Azzi, V. D., and Tsai, S. W., 1965, "Anisotropic Strength of Components," Exp. Mech., **5**, pp. 286–288.
[51] Vinson, J. R., and Sierakowski, R. L., 1987, *The Behavior of Structures Composed of Composite Materials*, Martinus Nijhoff, Leiden, The Netherlands.
[52] Press, W. H., Flannery, B. P., Teukolsky, S. A., and Vetterling, W. T., 1990, *Numerical Recipes: The Art of Scientific Computing* (FORTRAN Version), Cambridge University Press, Cambridge, UK.
[53] Stewart, G. W., 1970, *Introduction to Matrix Computation*, Academic, New York.
[54] Stoer, J., and Bulirsch, R., 1980, *Introduction to Numerical Analysis*, Springer, New York, Article 6.7.
[55] Cumpsty, N. A., 1989, *Compressor Aerodynamics*, Longman Scientific and Technical, Essex, UK, Chap. 10.
[56] Cumpsty, N. A., 1992, "Aerodynamics of Aircraft Engines—Stride and Stumbles," M.I.T., Cambridge, MA, GTL Report 213.
[57] Walsh, P. P., and Fletcher, P., 2004, *Gas Turbine Performance*, Blackwell Science, Oxford, UK.
[58] Kerrebrock, J. L., 1992, *Aircraft Engines and Gas Turbines*, 2nd ed., The MIT Press, Cambridge, MA.
[59] Khalak, A, 2002, "A Framework for Flutter Clearance of Aeroengine Blades," ASME J. Eng. Gas Turbines Power, **124**, pp. 1003–1010.
[60] Armstrong, E. K., and Stevenson, M. A., 1960, "Some Practical Aspects of Compressor Blade Vibration," J. R. Aeronaut. Soc., **64**, pp. 117–130.
[61] Kielb, R. E., 1993, "Turbomachinery Aaeroelasticity," Lecture Notes and Private Communication. Structural Mechanics Lecture Series, Georgia Institute of Technology, Atlanta, GA.
[62] Fleeter, S., and Jay, R. L., 1987, "Unsteady Aerodynamic Measurements in Flutter Research," AGARD Manual No. AG-298, Aeroelasticity of Axial-Flow Turbomachines, Volume 1: Unsteady Turbomachinery Aerodynamics.
[63] Jay, R. L., and Fleeter, S., 1987, "Unsteady Aerodynamic Measurements in Forced Vibration Research," AGARD Manual No. AG-298, Aeroelasticity of Axial-Flow Turbomachines, Volume 1: Unsteady Turbomachinery Aerodynamics, NATO Science and Technology Organization.
[64] Azzi, V. D., and Tsai, S.W., 1965, "Anisotropic Strength of Composites," Exp. Mech., **5**, pp. 283–288.
[65] Dorn, W. S., 1960, "Duality in Quadratic Programming," Q. Appl. Math., **18**(2), pp. 155–162.
[66] Dorn, W. S., 1960, "A Duality Theorem for Convex Programs," IBM J. Res. Dev., **4**(4), pp. 407–413.
[67] Wolfe, P., 1963, "A Duality Theorem for Nonlinear Programming," Q. Appl. Math., **19**, pp. 239–244.
[68] Falk, J. E., 1967, "Lagrange Multipliers and Nonlinear Programming," J. Math. Anal. Appl., **19**, pp. 141–159.
[69] Fox, R. L., 1973, *Optimization Methods for Engineering Design*, Addison-Wesley, Reading, MA.
[70] Fleury, C., 1979, "Structural Weight Optimization by Dual Methods of Convex Programming," Int. J. Numer. Methods Eng., **14**(12), pp. 1761–1783.
[71] Fiacco, A. V., and McCormick, G. P., 1968, *Nonlinear Programming: Sequential Unconstrained Minimization Techniques*, John Wiley, New York.